Geometries, Driving Factors, And Connectivity Of Background Fractures At The Latemar Carbonate Platform (N. Italy): Relevance For Subsurface Reservoir Modelling

Onyedika Anthony Igbokwe[1, 2, *], Giovanni Bertotti[3], Mathias Mueller[1], Kelvin I. Chima[2, 4], and Adrian Immenhauser[1, 5]

Affiliation:

[1] Ruhr-University Boachum, Institute of Geology, Mineralogy and Geophysics, Universitätsstraße 150, 44801 Bochum, Germany

[2]Department of Physics, Geology and Geophysics, Alex Ekwueme Federal University Ndufu-Alike, Ikwo, P.M.B. 1010, Abakaliki, Ebonyi State, Nigeria

[3]Faculty of Civil Engineering and Geoscience, TU. Delft, Stevinweg 1, 2628 CN Delft, Netherlands

[4]Sorbonne Université-ISTeP UMR 7193, Paris, France

[5]Fraunhofer IEG (Institution for Energy Infrastructures and Geothermal Systems), Lennershofstrasse 140, 44801 Bochum, Germany

* Corresponding author. Email: `onyedikachi.igbokwe@rub.de`

Keywords: Background fractures; Conjugate fractures/veins; Latemar carbonate platform; Topology; Carbonate burial and/or subsidence trajectory.

Key Points:

- Background structures on the Latemar platform are constrained by three stress fields, forming two conjugate systems at different depths.
- Changes in the overburden influence the nature of formed background structures during burial and the spatial positions of principal stresses.
- The spatial and topological properties of fracture networks are different in lime- and dolostone pavements, informing subsurface fluid flow.

ABSTRACT

Carbonate platform background fracture networks are rarely utilized in subsurface models, and it is unclear how they relate to regional stress (other than faults and folds) and burial. We combine structural analysis and drone imagery to investigate the geometry, kinematics, and topological characteristics of (background) fractures at the Latemar platform (both limestones and dolostones; Northern Italy). Deformation was accommodated by a dense network of mode I and conjugate hybrid fractures/veins and conjugate reverse faults, all associated with sub-vertical stylolites. Conjugate fractures and associated subvertical stylolites are organized in two systems, constraining the major stress fields. Differences lie in the permutation of the position in the space of the principal stress with depth. Specific burial depth windows are significant in distinguishing the different spatial positions of the principal stresses. Changes

in overburden provide the major driving factor in determining the position of background structures that develop during the burial trajectory. Topologically, background fractures in lime- and dolostone pavements show distinct characteristics. In limestone pavements, fractures form a network with a high proportion of I-node and I-C to C-C branches, resulting in a low to moderate connectivity (i.e., $C_B = \sim 1.5$). In dolostones, a complex network with abundant Y-to X-nodes and I-C to C-C branches is found (moderate to a high degree of connectivity $C_B = \sim 1.7$). Topological pathways provide important insights into how background fractures are connected and shed light on the significance of these features in the context of subsurface fluid flow.

Plain Language Summary

Background fracture networks in carbonate platforms are infrequently used in subsurface models. Little is known about their relationship to regional stress (other than faults and folds) and burial. The geometry, kinematics, and topological properties of (background) fractures at the Latemar platform (both limestones and dolostones; Northern Italy) are investigated using structural analysis and drone photographs. Deformation was accommodated by a dense network of opening mode, conjugate hybrid fractures/veins, and conjugate reverse faults, all associated with sub-vertical stylolites. The principal stress fields responsible for the deformation and/or formation of fracture networks are constrained by two systems of conjugate fractures and related sub-vertical stylolites. Differential positions of principal stress in relation to depth in the major stress fields space distinguish the two systems. Changes in the overburden determine the position of background structures that develop during the burial trajectory.

Topologically, the background fractures in lime- and dolostone pavements are different regarding their connectedness in nodes and branches. Limestone pavements show relatively low-to-moderate connectivity compared to the dolostone counterpart with moderate-to-high connectivity. Topological pathways tell us a lot about how background fractures are connected and what these features mean for fluid flow at the subsurface.

1. Introduction

Natural fractures are common in carbonate reservoirs and are crucial for reservoir performance as conduits for fluid flow and in terms of fracture-related pore space and permeability (de Graaf et al., 2017; Lavenu et al., 2014). The number of fractures affecting carbonate reservoirs can be grouped into (i) background fractures formed during subsidence and linked with regional stresses and (ii) those associated with tectonic events, faults, or folds. This paper focuses on background fractures in carbonate rocks. These fractures are often regularly distributed throughout the hostrock and developed in response to regional stresses and/or subsidence and burial without the influence of faults or folds (Casini et al., 2011; Korneva et al., 2014; Lamarche et al., 2012; Lavenu et al., 2014, 2015). Typically, background fractures have variable spacing and lengths (heights) distribution (cm's-up to m's-scale), forming heterogeneous fracture networks (e.g.,

Boro et al., 2013; Casini et al., 2011; de Graaf et al., 2017; Lavenu et al., 2014), and can significantly increase the rock's natural permeability when open. Fractures that are fully occluded by cement, in contrast, may form near-impermeable fluid barriers (Laubach, 2003).

Carbonate reservoir models require accurate input parameters with regard to sub-seismic background fracture systems in order to distinguish between fractures of different mechanical origin. Essentially, the controls for the development of fractures reflect the type of structures (or deformation features) that will form and their position. For example, the structural elements in mode I and hybrid fractures or stylolites control the positions of the principal stresses. We follow previous critics of combing these features together in reservoir models without further recourse to the conditions of their formation and associated stress information (Bertotti et al., 2017; Bisdom et al., 2017; Bruna et al., 2019). The combination of mode I and hybrid fractures or stylolites in the reservoir models suggests that, despite significant progress, geoscientists and engineers lack important 'tools' to predict the occurrence of these features in buried platforms. Particularly, in an anisotropic rock body, such as the case of an isolated carbonate platform, these problems become most apparent. This is because these features are affected by various degrees of karstic overprint and hydrothermal fluids, potentially leading to limestone-dolostone neomorphism (Christ et al., 2012; Jacquemyn et al., 2014). All of these processes lead to significant lateral and stratigraphic changes in rock properties.

In rock bodies, where major faults and folds are absent, other studies have shown that fractures occur in otherwise undeformed carbonate rocks (Lamarche et al., 2012; Lavenu et al., 2014, 2015). For instance, carbonates deposited in shallow marine environments tend to lithify at an early diagenetic stage and enter the shallow burial as semi-lithified (but still very porous) rocks (Eberli et al., 2003; Ge et al., 2020; Lamarche et al., 2012). These brittle rocks are prone to fracturing at shallow depths due to localization of displacement and strain and/or induced by compaction or tectonic forces. As such, even in the absence of faults and folds, background fracturing can take place during subsidence and burial (e.g., Bisdom, 2016; Casini et al., 2011).

The reservoir analog dealt with in this paper is the celebrated Latemar carbonate platform in Northern Italy (The Dolomites), which is a very intensely studied outcrop (Boro et al., 2013, 2014; Christ et al., 2012; Emmerich et al., 2005; Goldhammer et al., 1990; Hardebol et al., 2015; Jacquemyn et al., 2014, 2015). The Latemar is an isolated carbonate atoll (Fig. 1a) and can serve as an analog of a subsurface reservoir. The Latemar is a particularly compelling study object, as it is one of the few preserved limestone atolls in the Dolomites. Moreover, it is riddled with hydrothermal dolomite bodies and dikes crosscutting the platform, all of these being related to Predazzo Intrusion (Carmichael & Ferry, 2008; Jacquemyn et al., 2014, 2015). This allows for studies comparing lateral changes between limestone and dolostone rock bodies in the m's to 10's of m's scale and structural changes across different stratigraphic domains (from bottom to top

of the platform).

This paper aims to: (i) characterize background fractures in terms of geometry, kinematics and chronology, (ii) understand what drives up background structures formed in platform carbonates related to the position of the principal stresses, and (iii) quantify the way fractures interact and connect within the two distinct lithologies (limestones and dolostones), which have undergone the same geodynamic history in Latemar. We explore the differences and similarities in connectivity and complexity of the fracture networks in both lithologies. Finally, we extrapolate the results to discuss the development of background fractures in platform carbonates, changes in stress state through time, and topological variabilities by using the studied example as a proxy.

1. The latemar atoll: case setting

(a) Geotectonic history

The Latemar carbonate atoll is one of the pre-volcanic Late-Anisian-Ladinian isolated carbonate platforms (Goldhammer & Harris, 1989; Preto et al., 2011) located in the southwestern part of the Dolomite Mountain belt (northern Italy; Fig. 1a, b). The Latemar forms part of the Southern Alps, which, in turn, are a segment of the Mesozoic Adriatic plate, involved in predominantly southward thrusting during the Alpine collision between Africa and Europe (e.g., Boro et al., 2013; Doglioni, 1988).

In what forms today the Dolomites Mountain belt, a broad and extensive carbonate ramp developed (Contrin Formation; Ruffer & Zuhlke, 1995). The large-scale carbonate ramp was fragmented into several horst and graben structures by the overall extensional faulting in the Late Anisian (Castellarin et al., 1988; Gaetani et al., 1981; Preto et al., 2011). Between the Late Anisian and Late Ladinian (Middle Triassic), a series of isolated carbonate buildups, including the Latemar platform (Schlern Formation; Bosellini, 1984; Fig. 1b), formed on topographic highs. These buildups were separated by basinal areas recording the deposition of siliceous, open-marine carbonates. Following a regional magmatic-tectonic event in the Late Ladininan to Early Carnian, massive magmatic activity triggered the intrusion of the Predazzo Volcanic-Plutonic Complex and the Mt. Monzoni intrusion (Fig. 1c; Bellieni et al., 2010; Bosellini, 1984; Bosellini et al., 2003). Carbonate deposition came temporarily to a halt, mainly when Wengen Group's volcanic covered most of the platform top and parts of the surrounding basins and flank deposits (Bosellini, 1984; Bosellini, 1996). Dikes radiating from the Predazzo intrusion into the Latemar carbonate edifice are mainly monzonitic in composition (Visona, 1997) and emplaced between 232 – 238 Ma (Laurenzi & Visona, 1996). The majority of these dikes are oriented sub-vertically, and their strike has a 325^{o} azimuth (Jacquemyn et al., 2015).

1. The Latemar

The Latemar is impacted by the syn-sedimentary tectonic processes in the Middle Triassic and the later Alpine tectonics (Preto et al., 2011). The current

morphology of Latemar has a maximum altitude of 2850 m, with the high peaks exposing extensive parts of the platform interior, the margin, and the slope (Figs. 1 and 2). The platform interior, a 720 m succession of subtidal and peritidal carbonate lagoonal deposits (Egenhoff et al., 1999), is arranged in dm's-to m's-scale shallowing upward cycles (Christ et al., 2012; Goldhammer et al., 1990). The platform margin, which is scarcely preserved, comprises massive reefal boundstones, extensive microbial crust, and abundant marine cement (Emmerich et al., 2005; Goldhammer & Harris, 1989; Harris, 1993, 1994; Marangon et al., 2011). The slope is characterized by massive breccia flows, including coarse and matrix-poor materials derived from the platform margin or platform interior (Egenhoff et al., 1999; Harris, 1994). Although the Latemar platform belongs to the groups of the pre-volcanic platforms that preserved a predominantly calcite mineralogy, a sizeable volume of hydrothermal dolomites is present. The dolomitization of the Latemar is primarily linked to fluids and contact metamorphism related to the Predazzo intrusion forming a contact aureole with (de)dolomite marbles and, most prominently, hydrothermal activity related to magmatic dikes (Visona, 1997; Carmichael and Ferry, 2008; Jacquemyn et al., 2014; Mueller et al., 2021). Dolomitizing fluids circulated along the pathways of the numerous mafic dikes and caused the spatial hydrothermal dolomitization of the formerly calcitic Latemar carbonates.

Structural studies focusing on the Latemar platform, essentially fracture-related ones, have been performed (Boro et al., 2013, 2014; Preto et al., 2011). These study document that a large number of volcanic dikes strike NNW-SSE, and a limited number of strike-slip and normal faults generally oriented NNW-SSE, and NNE-SSW traverses the platform. Typically, these faults are of Middle Triassic (Anisian) to Alpine (Neogene) in age, with high angle Alpine faults commonly reactivating pre-existing planes. This reactivation is acknowledged by the presence of striation on some joint surfaces and surfaces bounding volcanic dikes (Gramigna et al., 2013). Despite evidence for the reactivation, however, the Alpine tectonic scarcely overprinted the original sedimentary architecture of the carbonate massif. Besides, opening mode fractures or joints and fracture corridors have also been identified. These structures are primarily oriented in two perpendicular sets, NNW-SSE and ENE-WSW, trending fractures (Boro et al., 2013; Preto et al., 2011).

1. Data set and fracture analysis

We investigated an approximately 2 x 3 km large study area on the Latemar platform, including outcrops in the Valsorda valley, which is 100's of m's lower than the platform top (Fig. 2). Distributed fractures with varying patterns were identified in lime- and dolostones and documented. We did not recognize prominent folds and/or faults. Exposures in the study area are generally of high quality. Outcrop stations (Figs. 1c and 2, and Table 1) were broadly grouped into three domains based on their stratigraphic position and structural styles for analysis. This grouping enables building a range of structural transects to understand the platform's deformational history from the base to the top of the

Latemar platform. (Fig. 1). We do not follow previously defined sedimentological lithozone classifications in every detail (see, e.g., Egenhoff et al., 1999; Goldhammer & Harris, 1989). Instead, we divided the outcrop stations into domains based on the observed changes in stratigraphic positions and structures, from the bottom to the platform's top.

The first domain (D1), near the steep southward-facing slope (present-day) of the Latemar Mountain, is located between 1.600 and 2.350 m a.s.l. in the Valsorda valley (D1 in Fig. 1d). There, bedding perpendicular outcrop stations, ranging from a few m's to 10's meters, are studied. The second domain (D2) lies between 2.400 and 2.600 m a.s.l. at the upper levels of D1 exposed at the center of the morphological 'amphitheater' of the central Latemar (Latemar interior). 'Latemar interior' represents the intermediate level of the Latemar, and both bedding parallel (pavement) and bedding perpendicular outcrop stations were studied (D2 in Fig. 1d). The third domain (D3) is situated at the highest part of the platform, located between 2.700 and 2.850 m a.s.l. (D3 in Fig. 1d) near the Rifugio di Pisa and Cima Feudo areas (Fig. 1c). Both bedding perpendicular and bedding parallel outcrop stations were studied.

Distributed fractures (and veins) were photographed, mapped, and structurally characterized within the exposed outcrop stations in all the domains. Data compiled include plane orientation and displacements (Fig. 3). Specifically, at the sub-horizontal outcrop (pavement) in D2, the fracture network patterns were acquired from stitched, and ortho-rectified images obtained using drone imagery (DJI Phantom 4®). The acquired images were processed using Agisoft Photoscan® and converted into georeferenced digital outcrop models using photogrammetry. Drone images were used to guide fieldwork on the ground to document minute structural details that were only in part visible in drone images. Spatial and dimensional attributes of fractures were collected from lime- and dolostones. These fractures and the stylolites were analyzed for their geometry, kinematics, and topology to delineate crosscutting relationships and the accompanying stress directions. We dedicated particular attention to the kinematics of veins and their relationships with both bedding-perpendicular and bedding-parallel stylolites. Interpretation and digitization of the observed fractures were carried out using ArcGIS 10.5^{TM} software. Fractures were traced and digitized using the polyline interpretation tool. The fractures were then analyzed for their geometric and topological characteristics using NetworkGT (Nyberg et al., 2018). Various tools within ArcGIS 10.5^{TM} focus on three aspects of two-dimensional fracture network analysis (sampling, geometry, and topology).

To understand fracture topology, which describes the geometrical relationships and arrangement of fractures within a network to determine their connectivity (e.g., Manzocchi, 2002; Sanderson & Nixon, 2015), we follow Sanderson and Nixon (2015) in adopting their view that fracture arrays are made of nodes and branches. Nodes are classified into I-, Y-, and X-nodes, representing respective points where a fracture terminates, abuts/splays against another fracture,

and/or intersects with another fracture. Branches are the portions of a fracture confined between two nodes. These are defined as isolated I-I branches, singly connected I-C branches, or doubly connected C-C branches if they are delimited by; two I-, one I-, and Y- or X-, and Y- and X-nodes respectively (Fig. 4a; Sanderson & Nixon, 2015, 2018). The proportion of different node and branch types describes the network topology. Once the number of nodes and/or branches making up fracture arrays is known, the connectivity can be quantified and visualized in a ternary plot of the component proportions. This entails measuring the number of connections per branch $n\mathrm{C_B}$ ranging from 0 to 2. The value 2 signifies a very high and/or perfectly connected network (Fig. 4b, c; for details of the mathematical derivation, see Sanderson & Nixon, 2015).

Finally, fractures' spatial heterogeneity was computed through transect lines, which lie perpendicular to each fracture cluster by relating a cumulative plot to a uniform distribution (Fig. 4d). A plot of cumulative frequency against distance from the beginning of the transect line allows a quick visual comparison of the distribution of different fracture populations and between transect lines with different lengths or fracture frequencies. For instance, the maximum deviation above (D+) and below (D-) the normal distribution are added to give a parameter V, for fracture frequency (Vf), i.e., V = D+ + D- (Fig. 4d). The V value ranges from 0 to 1 (representing homogenous to heterogeneous spacing distribution) upon normalizing the added deviations by cumulative total. For a more detailed description, see Nixon et al. (2019), Putz-Perrier & Sanderson (2008a, 2008b), and Sanderson & Peacock (2019).

1. **Results**

   (a) **Spatial distribution of structural elements and their characteristics across domains**

In the following, we describe the distribution of the structural elements in the area of study, focusing on the three outcrop domains: from bottom to top, the D1, D2, and D3 (see Figs. 1 and 2). Generally, in all the domains, the field investigations show widespread brittle deformation features across the limestones and their dolomitized equivalents. The dominant features within these rock types are low-strain barren fractures and/or veins, displayed as mode I and conjugate hybrid fractures/veins. Features containing significant strain are scarce and commonly limited to a few low-angle conjugate reverse faults, normal and strike-slip faults with a displacement of a few cms. Only very few fractures are striated. Besides the barren fractures and veins, sub-horizontal and sub-vertical stylolites (some cm's to a few m's long) are observed.

In analyzing the structural elements in each domain, especially the distribution of conjugate fractures, we consider the conjugate pattern's 'building blocks' mainly composed of two conjugate fractures/veins and the associated sub-vertical (tectonic) stylolites, referred to here as Conjugate System (CS). Two conjugate systems (CS1 and CS2) groups are distinguished and documented, measuring dihedral angles between 18 and 60°, and the conjugate kinematics

are consistent for the measured fractures.

The first domain (D1) is situated at the platform's base between 1.600 m a.s.l., in the Valsorda valley area (Fig. 5) and 2.350 m a.s.l., within the vicinity of San de Montagana (Fig. 6), respectively. In this domain, the Latemar carbonate edifice is affected by minor reverse faults dipping at low-angle ($< 30^{o}$) to bedding (Figs. 5 and 6). Four representative outcrop stations displayed both in the NNW and NNE flanks of the Valsorda valley and in the vicinity of San de Montagana, for example, figures 5a – e, 6 and Table 1, show that these low-angle reverse faults: (i) occur in conjugate sets, (ii) strike between *ca* 238^{o} WSW-ENE and 250^{o} SW-NE, and (iii) accommodate low-angle SSE - and ENE dipping fractures with a horizontal intersection. The kinematic indicators on the low-angle conjugate reverse fault planes point to dip-slip motion. Displacement is commonly minimal (a few cm) with a poorly developed damage zone and minimal fault core thickness whenever they are present. Besides the conjugate reverse faults, sub-horizontal barren fractures (bedding-parallel mode I), sub-horizontal stylolites, and sub-vertical stylolites were also observed specifically in figure 5d, f, g. In particular, the sub-horizontal stylolites, ranging in length from cms to 10's of cms, exhibit less well-developed peaks when compared to their sub-vertical counterpart, which ranges in height from cms to a few meters, having a well-developed peak.

The sub-vertical stylolites are oriented primarily on *ca* 230 to 250^{o} NE-SW to ENE-WSW and strike perpendicular to the maximum sub-horizontal stress. These sub-vertical stylolites, coupled with the orientation of low-angle conjugate reverse faults, determined an approximate N-S to NNW-SSE trending sub-horizontal 1 stress (Figs. 3, 5, and 6).

Overall, the structural configurations documented in D1 constrain the orientation of the principal stresses into sub-horizontal 1 (N-S to NNW-SSE) and 2, and sub-vertical 3. This configuration constitutes the CS1.

The second domain (D2) is located at the center of the morphological 'amphitheater' of the Latemar between 2.400 and 2.600 m a.s.l., also referred to as a flat-topped central portion inner platform (e.g., Marangon et al., 2011; Preto et al., 2011). Here, drone imagery and field studies document fractured bedding-parallel (pavement) and bedding-perpendicular outcrops covering lime- and dolostone lithologies (Figs. 1d, e and 7).

In this domain, the sub-vertical conjugate fracture/vein sets strike predominantly in the NE-SW and ENE-WS directions for both, lime- and dolostone lithologies (e.g., Figs. 7, 8, and 9). Further, the sub-vertical stylolites, for the most part: (i) show a striking direction, approximately NW-SE to NNW-SSE, (ii) range in length from cm up to a few meters, (iii) have less well-developed peaks, and (iv) associate with a NE-SW to ENE-WSW trending sub-horizontal 1 stress (e.g., Figs. 3i - iii, 8, and 9 of stations, LAT_Gi, Gii and Giii). The NE-SW to ENE-WSW sub-horizontal 1 stress is compatible with the observed conjugate hybrid fractures/veins (generally striking NE to ENE direction) for

which sinistral and dextral senses of movement are determined (Figs. 8 and 9). In this domain, the structural configuration within the lime- and dolostone lithologies at the pavement outcrop stations constrain the orientation of the principal stresses into (i) sub-horizontal 1 (NE-SW to ENE-WSW) and 3, and (ii) sub-vertical 2. These constitute the CS2.

Besides the bedding parallel outcrops, many examples of bedding-perpendicular outcrops in this domain show the occurrence of a few abundant sub-horizontal stylolites, pointing to compression normal to bedding. The sub-horizontal stylolites, like in D1, vary in lengths, ranging from a few cm up to a few meters. Unlike in D1, the sub-horizontal stylolites overprint the conjugate fracture sets, which are observed to belong to CS2.

The third domain (D3) is stratigraphically in the higher part of the platform between 2.700 and 2.850 m a.s.l., precisely at the Rifugio di Pisa (Fig. 1c, d). Structures and/or features observed in the studied outcrop stations (e.g., Figs. 10, 11, and 12) are displayed as mode I and conjugate hybrid fractures and stylolites, including sub-horizontal and sub-vertical ones. For instance, considering the bedding parallel outcrops, in figure 10, fractures are arranged in conjugate patterns along two main orientations: NE-SW and ENE-WSW. The conjugate fractures/veins are co-genetic with the NW-SE to NNW-SSE trending sub-vertical stylolites.

Further, the ENE-WSW-oriented fractures are the dominant fracture set on the bedding-perpendicular outcrops (Figs. 11 and 12). Also, the sub-vertical and sub-horizontal stylolites on these outcrops range in length from cms-up to several meters tall and long, respectively.

The sub-vertical stylolites are widely spaced, and abut against bedding surfaces dipping toward the NE. These stylolites, coupled with the intersection of the two biaxial planes of the conjugate fractures, document predominantly ~ a NE-SW to ENE-WSW trending sub-horizontal 1.

Conversely, the sub-horizontal counterpart varies in spacing between 2 and 3 cm and several meters (e.g., Figs. 11 and 12). Where the spacing between the sub-horizontal stylolites is small, these are often interconnected, creating a network of dense branching stylolites (Fig. 12h, g). In addition, the sub-horizontal stylolites overprint the conjugate fractures/veins belonging to CS2, and in rare occasions, abut against the veins that do not form in the conjugate pattern (Fig. 11). Close-up observation shows that the sub-horizontal stylolites overprint the sub-vertical ENE-WSW oriented stylolites (Fig. 12). Other than that, some veins seem to overprint or mutually crosscut the sub-horizontal stylolites (Fig. 11c). Most of these veins form later, as they are seen to respond to the sub-vertical maximum principal stress, which leads to the development of the sub-horizontal stylolites.

1. **The overall structural configurations in all domains**

The cumulative result of the overall structural configurations in all the three

domains as described above is shown in figure 13. These different structural elements are reflected in: (i) The conjugate systems in each domain, for example, CS1 and CS2, constrained for D1 and D2, D3, respectively (Fig. 13a). (ii) The orientation of the sub-vertical stylolites perpendicularly bisecting the conjugate fractures. Two groups of sub-vertical stylolites are observed, namely the NE-SW to ENE-WSW and NW-SE to NNW-SSE directed ones, which are predominant in D1 and D2, D3, respectively (Fig. 13b). (iii) The direction of the sub-horizontal 1 stress, which in D1 is primarily at NNW-SSE and, in D2, D3, tends towards the NE-SW to ENE-WSW direction. (iv) The frequency (abundance) of the sub-horizontal stylolites. While D1 constrain CS1 and bedding parallel mode I fracture predominantly, D2 and D3 have a dense network of mostly interconnected sub-horizontal stylolites overprinting conjugate hybrid fractures belonging to CS2.

1. **Fracture networks' spatial heterogeneity and intensity in lime- and dolostones at the pavement of D2**

In the following, the fracture networks' spatial heterogeneity and intensity (length of fracture trace/area of exposure) within the lime- and dolostones at D2 are presented. The results focus on the two predominant fracture populations, ENE-WSW and NNW-SSE, shared within the lime- and dolostones at D2 (e.g., Fig. 7). The length distributions of these fracture populations, using a series of cumulative frequency plots (negative exponential and power-law) and tables of fracture statistics, are shown in figures 14c, d, g, h. From the drone imagery of the fractured sub-horizontal outcrop stations (pavements), four (4) out of a total of fourteen (14) measured line transects of cumulative frequency are described, including changes in the fracture intensities between the lithologies.

With respect to the ENE-WSW fractures, the transects of two sub-vertical 4.5 and 7.5 m lines (Te and Tm; Fig. 7a, d) intercept ~ 35 and 25 fractures in lime- and dolostone pavements, respectively. The fracture's median spacings (0.07 and 0.22 m; Fig. 14a, e) are slightly less than their average spacings (0.11 and 0.33 m). The cumulative plots and associated V-values (Fig. 13) show a slight increase in heterogeneity from limestone (e.g., Te; Figs. 7a and 14a) to dolostone (e.g., Tm; Figs. 7d and 14e). This increase is also reflected in fracture frequency (Vf), with V-values increasing from 0.15 to 0.24 (Fig. 14a, e).

With regard to the NNW-SSE fractures, the 6- and 10-m-long transects (e.g., Tf and Tn; Fig. 7a, d) comprised 47 and 20 fractures in both lime- and dolostone pavements, respectively. The NNW-SSE fractures median spacing (0.10 and 0.25 m) are less than their average spacing (0.13 and 0.45 m). The cumulative plots and associated V-values show a slight increase in heterogeneity between lime- (Tf; Fig. 14b) and dolostone lithologies (Tn; Fig. 14d). The fracture frequency (Vf) values increase from 0.16 to 0.44 (Fig. 15b, f). Thus, for both the ENE-WSW and NNW-SSE fractures in lime-and dolostone, the length distributions fit perfectly to the negative exponential and power-law plots (Fig. 14c, d, g, h), pointing to closely spaced fractures.

Concerning the fracture intensities, for limestone pavements, the values range from 9 to 33 m^{-1} (LST_2) and 10 to 23 m^{-1} (LST_3) (Fig. 15a, b). In comparison, the local fracture intensities for the corresponding dolostone pavements range from 3 to 18 m^{-1} (DST_2) and 2 to 14.1 m^{-1} (DST_3) (Fig. 15c, d). In both lithologies, the highest intensity values positively correlate to areas where the fractures are either splaying, abutting, or crosscutting.

1. **Fracture topology and connectivity**

The mapped fracture patterns of both lime- and dolostones at the bedding parallel outcrops (pavements) of D2 (Fig. 7) show a varying degree of structural complexity. These complexities include overlapping fracture segments, stepping, abutting, splaying, crosscutting and interacting fractures. The structural styles within the pavements are further classified based on a change in the fracture topology and intersections.

The ternary diagrams in figure 16, along with Table 2, highlight the proportions of different node and branch types for each studied limestone (LST_2 and LST_3) and dolostone (DST_2 and DST_3) pavements. The lines contoured onto the ternary diagrams show thresholds for the number of connections per branch (nC_B) ranging from 0 to 2. For limestones, this number ranges between 1.52 and 1.55 (Fig. 16b) for LST_2 and LST_3. For dolostones, the values are 1.74 and 1.64 (Fig. 16d) for DST_2 and DST_3, respectively. These high values for dolostones are primarily a consequence of intersecting, splaying and crosscutting fractures.

For the node topology, limestone pavements plot closer to the *I*-node portion of the node ternary diagram compared to dolostone pavements (Fig. 16a, b). For instance, LST_2 and LST_3 (limestone pavements) show a large spread in node topology, having the proportion of *I*-nodes ~ 52 and 51%, respectively. In contrast, for dolostone pavements, DST_2 and DST_3, *Y*-nodes dominate, with DST_2 showing a large proportion of connecting nodes (> 65% *Y*- and *X*-nodes; Fig. 16c and Table 2) than any of the studied pavements. Aside from the I and Y nodes, the limestone (LST_3) in some data also has more significant X-nodes (26%) than other pavements.

The branch ternary diagram shows that most of the pavements plot along the *IC*-*CC* part with a low proportion of *II*-branches, between ~ 2 and 7% (Fig. 16b, d and Table 2). Limestone (LST_2 and LST_3), exhibit more *IC*-branches (~ 30% and 31%) than the dolostone's DST_2 and DST_3 counterparts, i.e., ~ 22 and 24% respectively. Conversely, dolostone (DST_2 and DST_3) display more than 75% *CC*-branches, much greater than the limestone LST_2 and LST_3 pavement, i.e., up to 60%. These results point to a gradual rise in both the proportion of connecting nodes (*Y*- and *X*-nodes) and the *CC*-branches from lime- to dolostone pavements.

Figure 17 shows the connecting node frequencies with varied values in the studied lime- and dolostones pavements. It suggests a good correlation with the higher fracture intensities, depicting areas of complex structural zones.

1. **The tectonic evolution and the relative age of stress regimes at the latemar**

The geodynamic context responsible for creating high accommodation space in Latemar is associated with the late Anisian to early Ladinian extension, widely documented in the Dolomites and Eastern Southern Alps (Bertotti et al., 1993; Doglioni, 1988). Linking the orientations of principal stresses in which different natural fractures form (in the Ladinian times) at Latemar to the Andersonian stress regimes (fig. 18), observations in at least nine outcrop stations, for example, from D1 to D3, show three stress fields constrained by two different conjugate systems (Figs. 5 and 8). The first two stress fields (figs. 3 and 12) show sub-horizontal, roughly (i) N-S to NNW-SSE directed σ_1 and a sub-vertical σ_3, and (ii) NE-SW to ENE-WSW directed σ_1 and a sub-vertical σ_2. The third stress field shows a sub-vertical position of σ_1 (perpendicular to the orientation of sub-horizontal stylolites) and sub-horizontal σ_2 and σ_3. Whereas the first stress field is predominant at D1, corresponding to the reverse fault stress regime, the second and third stress fields are common at D2 and D3, consistent with strike-slip stress regimes. The differences in these stress fields lie in the permutation of the position in the space of the principal stress with depth.

Based on the crosscutting and abutment relations of structures, the relative age of the stress fields and the timing of the conjugate fractures' development show that the stress field associated with CS1 formed prior to those linked with CS2. The parallelism established between the conjugate fractures' development and Ladinian sub-volcanic dikes' that crosscut the Latemar in Boro et al. (2013), Jacquemyn et al. (2015), and Preto et al. (2011) implies that CS1 is Middle Triassic in age. The compatibility of the N-S to NNW-SSE directed sub-horizontal σ_1 with the Early Ladinian tectonic settings as documented in regional studies (e.g., Doglioni, 1984; Blendinger, 1986; Boro et al., 2013; Bosellini et al., 2003) further confirms the age of CS1 to Ladininan times, and these are primarily found in the outcrops exposed at D1 (Figs. 5 and 6). This event predates (i) the shifting of the stress fields from N-S to NNW-SSE towards the NE-SW to ENE-WSW sub-horizontal σ_1, which is responsible for the CS2, observed in most outcrops in D2 and D3, and (ii) the later sub-vertical σ_1, which formed the wide-ranging sub-horizontal stylolites throughout D2 and D3 locations (Figs 8, 9, and 10). These sub-horizontal stylolites crosscut the conjugate fractures of CS2 (Fig. 12). Meaning that the conjugate fractures must have formed first at a depth shallower than the sub-horizontal stylolites.

Overall, the structural evolution of the Latemar is interpreted to show primarily structures formed as a result of burial and/or subsidence impact on the carbonates. These impacts occur in a relatively common tectonic setting characterized by the presence of significant sub-horizontal stress of non-gravity origin and those resulting from gravity. Essentially during subsidence, the carbonates encounter different depth intervals and stress configurations at each interval. The resultant effect is the formation of diverse structures at each interval; see figures 5, 8 and 10. Thus, the tectonic evolution of the Latemar is characterized by the

first stage of distributed deformation, creating conjugates reverse fractures and veins followed by sinistral and dextral conjugate fractures and the development of perpendicular barren fractures, veins, and faults. Transpression along a N70E axis in the Dolomite mountain belt, the Stava Line-Cima Bocche Anticline (Fig. 1a; Doglioni, 1984) must have played a critical inherited geometry role during this evolution.

1. Discussion

In the following, we consider the collected structural data in terms of their mode, kinematics, orientations, abutting, and crosscutting relationship and include controlling factors and associated stress fields. These parameters are of general relevance for the structural modelling of sub-surface carbonate reservoirs.

1. Background fractures related to faulting of the Latemar

The Latemar platform's deformation caused the development of an extensive system of relatively clustered structures and/or fracture networks, which induce spatial anisotropy, especially in the pavement (sub-horizontal) dimension. Features such as (i) the sub-vertical mode I and hybrid fractures/veins and stylolites, and (ii) the sub-horizontal stylolites are present. These features are associated with three distinct stress fields: two sub-horizontal 1 (of different orientations) and overburden stresses. Data shown here suggest that many of the structures are accommodated in conjugate systems (e.g. CS1 and CS2). Each conjugate system is made up of two sets of sub-vertical hybrid fractures/veins, with sub-vertical stylolites bisecting the large angle between them and orientated parallel to their intersection.

In many carbonate platforms, deformation and fracturing of weakly to fully lithified carbonates are typically related to direct evidence of faulting and/or folding events in which their initial stages induce the development of extensive background fracture networks (e.g., Agosta & Aydin, 2006; Bosence, 2005; Petrullo et al., 2017; Tondi, 2007; Igbokwe et al., 2018, 2020). In contrast, in some platforms, background fractures develop instead in response to regional far-field stresses (e.g., Agosta et al., 2012; Casini et al., 2011; Korneva et al., 2014; Lamarche et al., 2012; Lavenu et al., 2014, 2015) and/or subsidence (Bertotti et al., 2017) without the influence of faults or folds.

In the Latemar platform, faults of Middle Triassic (Anisian) to Alpine (Neogene) age (Fig. 1 and 2) are accommodated. Although these faults have played essential roles in different stages of the structural evolution of the platform, the Alpine tectonics minimally affect the original sedimentary architecture of the Latemar carbonate massif despite their reactivation evidence (Gramigna et al., 2013). This implies that the impact of the Anisian faults related to the overall deformation of the Latemar can be elucidated in the present-day setting. For this reason, we are careful to separate the influence of these extensional tectonics during the Middle Triassic and the later impact of the Alpine compression in the Neogene.

Gramigna et al. (2013) and Preto et al. (2011) documented the characteristics of the Middle Triassic (Anisian) faults in Latemar as largely synsedimentary normal (conjugate) faults with extensional kinematics. These Anisian faults strike predominantly N40 – N60 or N100 – N120, and their tectonics are linked to the ongoing subsidence leading to the formation of the South Alpine passive continental margin (Bertotti et al., 1993; Fantoni et al., 2004). In the case of the study example presented here, we infer that the Anisian faults have minimal contribution to the formation of the initial background fractures. Our inference is based, for instance, on observations in three pavement outcrops (precisely at D2) where outcrops show mode I and the hybrid conjugate veins occluded by marine cement phases, specifically radiaxial fibrous calcite and dog tooth cement (e.g., Figs. 8, 10, and 11). These veins preserved a series of primary depositional features, have a dihedral angle of about 30^{o}, and are thought to have formed during subsidence and related burial (Boro et al., 2013; Jacquemyn et al., 2014, 2015; Preto et al., 2011; Mueller et al., 2021). This implies that these veins must have formed earlier at deposition, which is coeval with the emplacement of magmatic dikes at around 240 – 230 Ma. Additionally, the location of the Anisian faults *vis a vis* with the studied outcrops shows that the faults are far apart, at least 100s of meters, from the outcrop locations (Figs. 1 and 2). This is coupled with the apparent absence of folds in the vicinity of the study area. Consequently, with these facts, we propose that: (i) the Anisian faults may have no or minimal influence on the studied background fractures. (ii) the impact of far-field regional stresses must have initiated deformation during the subsidence, forming the different fractures/veins at depth, at least in the case of the studied fracture pavements.

In other places, sub-horizontal stresses have been documented in Berda and Kef Eddour formations in Tunisia (Bisdom et al., 2016, 2017), and the Jandaira Formation in Brazil (Bertotti et al., 2017), causing background conjugate fractures with low dihedral angles $< 30^{o}$. These fractures are thought to have formed during early horizontal contraction, particularly for the Berda and Kef Eddour formations in Tunisia, which also caused regional folding, thereby underlying the importance of layer parallel shortening (e.g., Ahmadhadi et al., 2008). The implication is that the background structures in Latemar must have formed earlier as the rock subsides, influenced by sub-horizontal (regional) stresses, prior to large-scale reactivation by later extensional and Alpine compressional tectonics, particularly in the Neogene.

1. **Background fractures in relation to overburden stress and changing positions of the principal stresses**

The position of background structures (fractures/veins and stylolites) depends on the principal stresses' spatial position. The principal stresses, in turn, depend on the depth at which the deformation takes place and the intensity of the tectonic (or sub-horizontal) stress. Our results show that the stress regime changes with depth, even when the intensity of the sub-horizontal stresses (including the applied boundary stresses) are constant. This situation presents

a challenge in knowing the type of structures, namely, mode I and/or hybrid fractures or stylolites, that will form as the rocks deform (or subside). Typically, when characterizing subsurface rocks used in reservoir models, the sets of structures (mode I, and hybrid fractures or stylolites) are essential, but these structures are mostly considered individually (e.g., Agosta et al., 2010, 2012; Panza et al., 2016; Giuffrida et al., 2019, 2020). This, in turn, implies that the associated stress information is obscured, resulting in inappropriate subsurface reservoir models. The questions of (i) how do the rocks (with reference to the Latemar) accommodate and react to different episodes of stress regime and, in particular, to subsidence or burial related deformation, and (ii) what possible structures will develop and at what depth, remain an open discussion. Here, we elucidated this by considering the structures in the two conjugate systems and documented stress fields.

A comparative analysis of the formation and changes in the conjugate systems' geometry, documenting three stress fields, is shown in figures 5, 8, 10 and 18. The documented differences between the first two stress fields lie in the principal stresses' changing positions (stress permutation), from reverse fault to strike-slip stress regimes. The third stress field is governed by sub-vertical 1, primarily influenced by the overburden.

Previous workers Bertotti et al. (2017) presented a model of subsiding carbonate rock, which envisages that the acting stress fields can be either gravity as the only force or combined gravity and the far-field sub-horizontal stresses. The sub-horizontal stresses can be of the tectonic origin or related to lateral pressure changes affecting the lateral thickness and density variations as, for example, found in some passive continental margins (Pascal & Cloetingh, 2009). These authors predicted three different depth intervals at which the conjugates, coupled with the position of the associated principal stresses, form in carbonate rocks during subsidence. Based on this, our estimate shows that the compression of the roughly N-S to NNW-SSE trending sub-horizontal 1, and a sub-vertical 3 (i.e., for CS1; Figs. 13a and 18a) took place at a relatively shallow to an intermediate burial depth of about 300 – 500 m. At this shallow depth, bedding-parallel mode I fractures, sub-vertical stylolites and/or low-angle reverse faults, (mainly in D1) formed (Figs. 5 and 6). Indirect evidence for this notion comes from the understanding that, in the presence of sub-horizontal tectonic stress, a sub-vertical position of 3 is compatible with low-angle reverse faults (or structures), and these form at shallow to intermediate burial depth (e.g., Bertotti et al., 2020; Bisdom et al., 2016a). Under ongoing subsidence, the Latemar platform's carbonates experienced intense fracturing and entered a depth interval characterized by a sub-vertical 2 and a sub-horizontal roughly NE-SW to ENE-WSW trending 1 (i.e., CS2; strike-slip stress regime; Figs. 13a and 18c). Because the vertical stress has substantially increased from 3 to 2, a dense network of sub-vertical mode I and conjugate hybrid fractures/veins and associated stylolites developed. These structures are common at D2 and D3 (Figs. 8, 9 and 10), and the burial depth at which this deformation took place is estimated to be not more than 500 – 800 m. The value of this depth interval

is similar to that proposed in Boersma et al. (2019) and Ebner et al. (2010).

Further subsidence of the deformed Latemar carbonate allows 1 to attain a vertical position – the third stress field. This stress field induces the activation of the wide-ranging sub-horizontal stylolites, formed primarily due to overburden compaction by gravity force (Figs. 12, 13, and 18d), mode I fractures (steep fractures/veins formed later) and normal faults. The sub-horizontal stylolites overprint the sub-vertical conjugate hybrid fractures/veins (Fig. 12a, e, i), and the NNW-SSE trending sub-vertical stylolites (Figs. 12c, d, g). This indicates that the formation of sub-horizontal stylolites occurred after the impact of the sub-horizontal compressional stresses that form the conjugate fractures. The dense fracture-stylolite patterns overprinting the conjugate hybrid fractures are similar to what has previously been described from subsiding carbonate rocks elsewhere (e.g. Bertotti et al., 2013, 2017; de Graaf et al., 2017; Boersma et al., 2019; Igbokwe et al., 2018, 2020). Given this, our results point to conjugate systems formed both at a shallower depth, as the platform deforms (or subsides), and at the intermediate, to greater depth, before the platform reaches its maximum burial depth. We noted some similarities in structures observed in the outcrops at D2 and D3 (Fig. 13a). These similarities suggest that these outcrops (at D2 and D3) belonged to the same package of layers during deposition and may have been affected by different erosional episodes and/or varying degrees of uplift. Meaning that the formation of structures in these domains corresponds more or less to the same time. On this note, we conclude that specific burial depth windows are important in characterizing the different spatial positions of the principal stresses by determining which of the principal stress coincides with the far-field stress or gravity. This, in turn, will determine the type of structural elements that will form.

At the surface level, the overburden stress has zero value. It then builds up at a proportion exceeding other stresses and which, at a specific depth, will inevitably become the maximum compressional stress. Therefore, changes in overburden provide the major driving factors in determining the type of background structures (e.g. mode I and conjugate hybrid fractures or stylolites) that develop in subsiding carbonate rocks.

1. **Role of hydrostatic pore pressure and stress concentration**

Previous workers (Roberts & Nunn, 1995; Sibson, 2003) linked the development of a dense network of sub-vertical mode I and conjugate hybrid fractures/veins to pore pressure. The hybrid nature of the fractures/veins documented here comes from the fact that: (i) most single fractures/veins are sheared, and (ii) the fractures/veins occur in conjugate patterns with low inter-fault angles (Hancock, 1985). Commonly, in a compressional stress regime, high pore pressure controls the activation of hybrid fractures in low porosity carbonate rocks, especially when the rock layers underlying the low porosity carbonate rocks are permeable (Sibson, 2003). In the case study presented here, the lithification of carbonates in the marine diagenetic domain and subsequent chemical and physical compaction during burial (e.g., Marangon et al., 2011) resulted in

low-porosity carbonate rocks in which these fractures formed. The underlying stratigraphic lower carbonate banks – belonging to Contrin and pre-Contrin formation (Fig. 1b, c) – of Latemar are not permeable (e.g., Carmichael and Ferry, 2008; Jacquemyn et al., 2014, 2015). Therefore, fractures formed at the Latemar could not have formed by increased high pore pressure emanating from these formations. The implications are that fractures in the Latemar platform must have remained mechanically open, i.e., did not close until occluded with carbonate cement. Assuming that these concepts hold, high hydrostatic pore pressure was not a significant factor affecting the formation of hybrid fractures in the Latemar platform.

Following Hancock (1985), Bisdom et al. (2016), and Bertotti et al. (2017), we propose that high-stress concentration due to increased depth and stress perturbation triggered the formation of hybrid fractures. As expected for lithified carbonate rocks, the concentration of stress increases with depth. This, in turn, changes the stress conditions due to stress perturbation and increases fracture frequency (Bai & Pollard, 2000; Boersma et al., 2020; Turcotte & Schubert, 2002).

Some degree of structural change has recently been linked with substantial modification in the flow pattern and chemistry of fluid (thought to be hydrothermal from the dikes) circulating in the Latemar. This is a result of a complex interplay of dissolution, precipitation, and cement paragenesis. The reader is referred to Mueller et al. (2021), the twin paper from this project, for detailed fluids and cement paragenesis documentation during the distributed deformation stages in Latemar.

1. **Spatial and topological variability of background fractures: implications for fluid flow**

The spatial arrangement of fracture arrays defines the structural heterogeneity and anisotropy in rock volumes and govern how fractures and faults affect fluid flow (Laubach et al., 2018). The differences in the spatial arrangements of fractures have significant implications for reservoir characterization inasmuch as fracture clusters, or sets of orthogonal fractures, can all contribute to fluid flow in the sub-surface (Li et al., 2018). As discussed in Laubach et al. (2018), the variation in fracture systems can occur when analyzed using scanline data, even within single sets. Here, we document a narrow range and spatial variability in the background fracture systems studied within the Latemar pavements at D2. There, the ENE-WSW and NNW-SSE fracture sets, common in both lime- and dolostone pavements show a regular anti-clustered distribution, indicating a lower variance in spacing as expected for uniformly distributed diffuse fractures. For instance, the low values of variation coefficients (Cv $>$ 1) and fracture frequency (Vf $>$1) for both ENE-WSW and NNW-SSE fracture sets within lime- and dolostone pavements, respectively illustrate only very minor or no changes in the distributed deformation (Fig. 14). Although, Nixon et al. (2014) found that fracture networks change their character within distributed deformation. Our results indicated that the studied fracture sets (ENE-WSW

and NNW-SSE) at D2 followed a similar length-frequency distribution in lime- and dolostone pavements. This implies that the multiscale dataset from these two lithologies is part of the same geodynamics system. Even so, we observed local changes in fracture character within dolostone pavements, where fractures largely branch and interact among themselves. This is because dolostones have different mechanical properties compared to their limestone counterpart. The characteristics of fracture interactions (clustered fracture network and homogenously distributed diffuse fractures) are constrained spatially but play a vital role in the flow network character (Hooker et al., 2013; Lamarche et al., 2012; Laubach et al., 2018; Manzocchi, 2002).

The topology application to the studied background fractures reveals distinct topological signatures characterizing both lime- and dolostones pavements (Figs. 16 and 17; Table 2). Representing these in quantitative terms for lime- and dolostone pavements show the average percentage values of the nodes and branches, respectively: (i) I (50.8 and 36.3%), Y (27 and 51%) to X (22.1 and 12.6%) nodes, and (ii) I-I (7.3 and 3%), I-C (31.1 and 23.3%) to C-C (59.9 and 71.6%) branches. Concerning connection-per-branch (C_B), the values for lime- and dolostones show 1.5 and 1.7, respectively. These representations reveal that the fracture networks in both lithologies are increasingly interacting and well-connected. In addition, these fracture networks show apparent similarity in their structural style and complexity in the sense of fracture intensity and orientation ranges (Figs 7 and 15), pointing to fractures formed in the same geodynamic system.

The high proportion of I-node and I-C to C-C branches in limestone pavements suggests a network generated by localized stress concentrations, accommodating decreased displacement at fracture tips (e.g., Shipton and Cowie, 2003; Nixon et al., 2020). Conversely, the abundance of Y-to X- nodes and I-C to C-C branches in dolostone pavements reveals a well-connected network. This connectivity of fractures allows fluids to follow their pathways, particularly in the complex zones where fracture intensities are high. The path provided by these fractures has contributed to supplying the hydrothermal fluids, especially within the numerous parallel dikes, that largely dolomitized the limestone at the Latemar platform. Similar relationships between the fracture network configuration (structural complexity) and topological characters were also described for carbonate platforms elsewhere (e.g., Duffy et al., 2017; Igbokwe et al., 2020; Morley & Nixon, 2016; Nixon et al., 2020). In all the studies, a higher proportion of Y-to X-nodes and I-C to C-C branches has important implications in evaluating the control exerted by the rocks on fluid migration in the subsurface.

Concluding, the distinct topologies of the background fractures allow the prediction of the different fracture network properties. These, in turn, can be useful when estimating deformation and fracture linkage in the subsurface. The similarities between these topologies in the Latemar platform in relation to other studied examples imply that the features documented in this paper might be more widely applicable with reference to larger-scale fracture and/or fault net-

works in carbonate platforms elsewhere.

1. **Conclusion**

Background fractures in both lime- and dolostone pavements in the Triassic Latemar platform interior have been mapped in detail and analyzed in terms of their geometry, kinematics, and topological characteristics. This has enabled us to document and quantify the background fracture network's structural complexity, arrangements, and connectivity. Further, the data shown here shed light on the manner in which background fractures form and vary spatially and topologically from lime- and dolostones.

Background fractures on the Latemar formed under the influence of three stress fields. The first two stress fields are characterized by sub-horizontal 1 and sub-vertical 3 or 2, ranging from reverse fault to strike-slip stress regimes. The sub-horizontal 1 is directed towards the N-S to NNW-SSE for the first stress field, with sub-vertical 3 and sub-horizontal 2, whereas, for the second stress field, NE-SW to ENE-WSW direction depicts the sub-horizontal 1 with sub-vertical 2 and sub-horizontal 3. These first two stress fields are responsible for conjugate systems (e.g., CS1 and CS2) at shallow to intermediate burial depths of perhaps 300 – 800 m, respectively. With further subsidence (> 800 m), the third stress field formed when the deformed Latemar carbonate allows 1 to attain a sub-vertical position. The formation of the third stress field initiates wide-ranging sub-horizontal stylolites, which developed primarily due to overburden compaction by gravity. The differences between the three stress fields lie in the permutation of the position in the space of the principal stress with depth. Therefore, changes in the overburden provide the major driving factor in predicting the nature of background structures, which will likely develop in subsiding carbonate rocks.

The structural style and complexity of the background fractures show distinct spatial and topological characteristics in lime- and dolostone studied pavements. Two fracture sets (NNW-SSE and ENE-WSW) are common to both lime- and dolostone pavements. These fractures show a regular anti-clustered distribution. Their lower variance in spacing (Cv > 1) and fracture frequency (Vf >1) illustrate only very minor or no changes in the distributed deformation.

Their networks include many isolated and a few splaying fractures. The fractures within the limestone pavements produce a network with a high proportion of I-node and I-C to C-C branches, resulting in a low to moderate degree of connectivity (i.e. CB = ~ 1.5). In contrast, fractures in dolostone pavements produce a more complex network with the abundancy of Y-to X- nodes and I-C to C-C branches. This results in a moderate to a high degree of connectivity (i.e. C_B = ~ 1.7), and their networks include well-connected and many crosscutting fracture components.

Background fractures in the Latemar platform provide an instructive example of the complexities inherent to their driving factors, formation, and stress configuration through time. The spatial and topological characteristics of fractures

provide a significant link to fluid-flow behavior by quantifying their fracture networks' structural arrangement and connectivity.

Acknowledgements

The Petroleum Technology Development Fund (PTDF) Abuja, Nigeria, is thanked for sponsoring the doctoral fellowship of the first author. The authors are grateful to A. Verdecchia for his assistance in flying the drone and generating the imagery, N. Gründken and S. Shurr for their assistance during the fieldwork. Thanks to O. Uwakwe for drawing some of the figures and J. Dikachi-Igbokwe for helpful comments, which helped improve this paper. The authors express their gratitude to the journal editor and reviewers…..

The datasets (original field photographs and drone images) presented here are drawn from the extensive fieldwork by the author(s) at the Latemar carbonate platform in northern Italy. These datasets, as captured in figures 5 through 12, can be accessed in the following data repository https://doi.org/10.5281/zenodo.6606860, where the images of different rock units riddled with diverse structural elements, including fractures (veins, joints, faults) and stylolites are stored. Drone images are processed using Agisoft PhotoScan® - a photogrammetry tool, in which the workflow is publicly available in the published work of Bisdom et al. (2017). Fracture datasets have been digitized, processed and analyzed geometrically and topologically using NetworkGT software, a toolbox developed for use in ArcGIS 5.1™. The toolbox is available for use under the GNU General Public License v3.0 and has been published in Nyberg et al. (2018). In addition, the geologic map of the study area, the cross-section profile and regional stratigraphic units (Figures 1a, b, c, and 2a) are available through published work by Gramigna et al. (2013), Preto et al. (2011) and Jacquemyn et al. (2014). The satellite data used in Figure 2b are from the Google Earth database and satellite images from bing maps (https://www.bing.com/maps/).

References

Agosta, F., Alessandroni, M., Antonellini, M., Tondi, E., & Giorgioni, M. (2010). From fractures to flow: A field-based quantitative analysis of an outcropping carbonate reservoir. *Tectonophysics*, *490*(3–4), 197–213. https://doi.org/10.1016/j.tecto.2010.05.005Agosta, Fabrizio, & Aydin, A. (2006). Architecture and deformation mechanism of a basin-bounding normal fault in Mesozoic platform carbonates, central Italy. *Journal of Structural Geology*, *28*(8), 1445–1467. https://doi.org/10.1016/j.jsg.2006.04.006Agosta, Fabrizio, Ruano, P., Rustichelli, A., Tondi, E., Galindo-Zaldívar, J., & Sanz de Galdeano, C. (2012). Inner structure and deformation mechanisms of normal faults in conglomerates and carbonate grainstones (Granada Basin, Betic Cordillera, Spain): Inferences on fault permeability. *Journal of Structural Geology*, *45*, 4–20. https://doi.org/10.1016/j.jsg.2012.04.003Ahmadhadi, F., Daniel, J. M., Azzizadeh, M., & Lacombe, O. (2008). Evidence for pre-folding vein development in the Oligo-Miocene Asmari Formation in the Central Zagros Fold Belt, Iran. *Tectonics*, *27*(1). https://doi.org/10.1029/2006TC001978Anderson, E. M.

(1905). The dynamics of faulting. *Transactions of the Edinburgh Geological Society*, *8*(3), 387–402. https://doi.org/10.1144/transed.8.3.387Bai, T., & Pollard, D. D. (2000). Fracture spacing in layered rocks: A new explanation based on the stress transition. *Journal of Structural Geology*. https://doi.org/10.1016/S0191-8141(99)00137-6Bellieni, G., Fioretti, A. M., Marzoli, A., & Visonà, D. (2010). Permo-Paleogene magmatism in the eastern Alps. *Rendiconti Lincei*, *21*(SUPPL. 1), 51–71. https://doi.org/10.1007/s12210-010-0095-zBertotti, G., Bezerra, F. H., Bisdom, K., Cazarin, C., & Reijmer, J. (2013, October 31). Outcropping Analogs and Multiscale Fracture Patterns in the Jandaíra Formation. *First EAGE/SBGf Workshop*. https://doi.org/10.3997/2214-4609.20131796Bertotti, Giovanni, Audra, P., Auler, A., Bezerra, F. H., de Hoop, S., Pontes, C., Prabhakaran, R., & Lima, R. (2020). The Morro Vermelho hypogenic karst system (Brazil): Stratigraphy, fractures, and flow in a carbonate strike-slip fault zone with implications for carbonate reservoirs. *AAPG Bulletin*, *104*(10), 2029–2050. https://doi.org/10.1306/05212019150Bertotti, Giovanni, de Graaf, S., Bisdom, K., Oskam, B., Vonhof, H. B., H. R. Bezerra, F., J. G. Reijmer, J., & L. Cazarin, C. (2017). Fracturing and fluid-flow during post-rift subsidence in carbonates of the Jandaíra Formation, Potiguar Basin, NE Brazil. *Basin Research*. https://doi.org/10.1111/bre.12246Bertotti, Giovanni, Picotti, V., Bernoulli, D., & Castellarin, A. (1993). From rifting to drifting: tectonic evolution of the South-Alpine upper crust from the Triassic to the Early Cretaceous. *Sedimentary Geology*, *86*(1–2), 53–76. https://doi.org/10.1016/0037-0738(93)90133-PBisdom, K., Nick, H. M., & Bertotti, G. (2017). An integrated workflow for stress and flow modelling using outcrop-derived discrete fracture networks. *Computers and Geosciences*. https://doi.org/10.1016/j.cageo.2017.02.019Bisdom, K, Bertotti, G., & Bezerra, F. H. (2017). Inter-well scale natural fracture geometry and permeability variations in low-deformation carbonate rocks. *Journal of Structural Geology*, *97*, 23–36. https://doi.org/10.1016/j.jsg.2017.02.011Bisdom, Kevin. (2016). *Burial-related fracturing in sub-horizontal and folded reservoirs: Geometry, geomechanics and impact on permeability*.Bisdom, Kevin, Bertotti, G., & Nick, H. M. (2016a). The impact of in-situ stress and outcrop-based fracture geometry on hydraulic aperture and upscaled permeability in fractured reservoirs. *Tectonophysics*. https://doi.org/10.1016/j.tecto.2016.04.006Bisdom, Kevin, Bertotti, G., & Nick, H. M. (2016b). The impact of in-situ stress and outcrop-based fracture geometry on hydraulic aperture and upscaled permeability in fractured reservoirs. *Tectonophysics*, *690*, 63–75. https://doi.org/10.1016/j.tecto.2016.04.006Blendinger, W. (1986). Isolated stationary carbonate platforms: the Middle Triassic (Ladinian) of the Marmolada area, Dolomites, Italy. *Sedimentology*, *33*(2), 159–183. https://doi.org/10.1111/j.1365-3091.1986.tb00530.xBoersma, Q. D., Douma, L. A. N. R., Bertotti, G., & Barnhoorn, A. (2020). Mechanical controls on horizontal stresses and fracture behaviour in layered rocks: A numerical sensitivity analysis. *Journal of Structural Geology*, *130*(July 2019), 103907. https://doi.org/10.1016/j.jsg.2019.103907Boersma, Q., Prabhakaran, R., Bezerra, F. H., & Bertotti, G. (2019). Linking natu-

ral fractures to karst cave development: A case study combining drone imagery, a natural cave network and numerical modelling. *Petroleum Geoscience*, *25*(4), 454–469. https://doi.org/10.1144/petgeo2018-151Boro, H, Bertotti, G., & Hardebol, N. J. (2013). Distributed fracturing affecting isolated carbonate platforms, the Latemar Platform Natural Laboratory (Dolomites, North Italy). *Marine and Petroleum Geology*, *40*, 69–84. https://doi.org/10.1016/j.marpetgeo.2012.09.012Boro, Herman, Rosero, E., & Bertotti, G. (2014). Fracture-network analysis of the Latemar Platform (northern Italy): Integrating outcrop studies to constrain the hydraulic properties of fractures in reservoir models. *Petroleum Geoscience*, *20*(1), 79–92. https://doi.org/10.1144/petgeo2013-007Bosellini, A. (1984). Progradation geometries of carbonate platforms: examples from the Triassic of the Dolomites, northern Italy. *Sedimentology*, *31*(1), 1–24. https://doi.org/10.1111/j.1365-3091.1984.tb00720.xBosellini, A., Gianolla, P., & Stefani, M. (2003). Geology of the Dolomites, an introduction. *Episodes*, *26*(3), 43. file:///D:/Dottorato back-up 04-04-2013/Bibliografia/Areas/Tethyan Realm/Southern Alps/DolomitesBosellini A. (1996). Geologia della Dolomiti. In *Casa Editrice Athesia, Bolzano-Bozen.*Bosence, D. (2005). A genetic classification of carbonate platforms based on their basinal and tectonic settings in the Cenozoic. *Sedimentary Geology*, *175*(1-4 SPEC. ISS.), 49–72. https://doi.org/10.1016/j.sedgeo.2004.12.030Bruna, P. O., Straubhaar, J., Prabhakaran, R., Bertotti, G., Bisdom, K., Mariethoz, G., & Meda, M. (2019). A new methodology to train fracture network simulation using multiple-point statistics. *Solid Earth*, *10*(2), 537–559. https://doi.org/10.5194/se-10-537-2019Carmichael, S. K., & Ferry, J. M. (2008). Formation of replacement dolomite in the Latemar carbonate buildup, Dolomites, northern Italy: Part 2. Origin of the dolomitizing fluid and the amount and duration of fluid flow. *American Journal of Science*, *308*(8), 885–904. https://doi.org/10.2475/08.2008.01Casini, G., Gillespie, P. A., Vergés, J., Romaire, I., Fernández, N., Casciello, E., Saura, E., Mehl, C., Homke, S., Embry, J. C., Aghajari, L., & Hunt, D. W. (2011). Sub-seismic fractures in foreland fold and thrust belts: Insight from the Lurestan Province, Zagros Mountains, Iran. *Petroleum Geoscience*, *17*(3), 263–282. https://doi.org/10.1144/1354-079310-043Castellarin, A., Lucchini, F., Rossi, P. L., Selli, L., & Simboli, G. (1988). The Middle Triassic magmatic-tectonic arc development in the Southern Alps. *Tectonophysics*, *146*(1–4), 79–89. https://doi.org/10.1016/0040-1951(88)90083-2Christ, N., Immenhauser, A., Amour, F., Mutti, M., Preston, R., Whitaker, F. F., Peterhänsel, A., Egenhoff, S. O., Dunn, P. A., & Agar, S. M. (2012). Triassic Latemar cycle tops - Subaerial exposure of platform carbonates under tropical arid climate. *Sedimentary Geology*, *265–266*, 1–29. https://doi.org/10.1016/j.sedgeo.2012.02.008de Graaf, S., Reijmer, J. J. G., Bertotti, G. V, Bezerra, F. H. R., Cazarin, C. L., Bisdom, K., & Vonhof, H. B. (2017). Fracturing and calcite cementation controlling fluid flow in the shallow-water carbonates of the Jandaíra Formation, Brazil. *Marine and Petroleum Geology*, *80*, 382–393. https://doi.org/10.1016/j.marpetgeo.2016.12.014Doglioni, C. (1984). Tet-

tonica Triassica Transpressiva nelle Dolomiti. *Giornale Di Geologia*, *46*(2), 47–60.Doglioni, C. (1988). Examples of strike-slip tectonics on platform-basin margins. *Tectonophysics*, *156*(3–4), 293–302. https://doi.org/10.1016/0040-1951(88)90066-2Duffy, O. B., Nixon, C. W., Bell, R. E., Jackson, C. A. L., Gawthorpe, R. L., Sanderson, D. J., & Whipp, P. S. (2017). The topology of evolving rift fault networks: Single-phase vs multi-phase rifts. *Journal of Structural Geology*, *96*, 192–202. https://doi.org/10.1016/j.jsg.2017.02.001Eberli, G. P., Baechle, G. T., Anselmetti, F. S., & Incze, M. L. (2003). Factors controlling elastic properties in carbonate sediments and rocks. *Leading Edge (Tulsa, OK)*, *22*(7), 654–660. https://doi.org/10.1190/1.1599691Ebner, M., Piazolo, S., Renard, F., & Koehn, D. (2010). Stylolite interfaces and surrounding matrix material: Nature and role of heterogeneities in roughness and microstructural development. *Journal of Structural Geology*. https://doi.org/10.1016/j.jsg.2010.06.014Egenhoff, S. O., Peterhänsel, A., Bechstädt, T., Zühlke, R., & Grötsch, J. (1999). Facies architecture of an isolated carbonate platform: Tracing the cycles of the Latemar (Middle Triassic, northern Italy). *Sedimentology*, *46*(5), 893–912. https://doi.org/10.1046/j.1365-3091.1999.00258.xEmmerich, A., Zamparelli, V., Bechstädt, T., & Zühlke, R. (2005). The reefal margin and slope of a Middle Triassic carbonate platform: The Latemar (Dolomites, Italy). *Facies*, *50*(3–4), 573–614. https://doi.org/10.1007/s10347-004-0033-6Fantoni, R., Bersezio, R., & Forcella, F. (2004). Alpine structure and deformation chronology at the Southern Alps-Po Plain border in Lombardy. *Italian Journal of Geosciences*, *123*(3), 463–476. https://pubs.geoscienceworld.org/italianjgeo/article/123/3/463/74893Gaetani, M., Fois, E., Jadoul, F., & Nicora, A. L. D. A. (1981). Nature and evolution of middle triassic carbonate buildups in the dolomites (Italy). *Marine Geology*, *44*, 25–57.Ge, Y., Pederson, C. L., Lokier, S. W., Traas, J. P., Nehrke, G., Neuser, R. D., Goetschl, K. E., & Immenhauser, A. (2020). Late Holocene to Recent aragonite-cemented transgressive lag deposits in the Abu Dhabi lagoon and intertidal sabkha. *Sedimentology*, *67*(5), 2426–2454. https://doi.org/10.1111/sed.12707Giuffrida, A., Agosta, F., Rustichelli, A., Panza, E., La Bruna, V., Eriksson, M., Torrieri, S., & Giorgioni, M. (2020). Fracture stratigraphy and DFN modelling of tight carbonates, the case study of the Lower Cretaceous carbonates exposed at the Monte Alpi (Basilicata, Italy). *Marine and Petroleum Geology*, *112*. https://doi.org/10.1016/j.marpetgeo.2019.104045Giuffrida, A., La Bruna, V., Castelluccio, P., Panza, E., Rustichelli, A., Tondi, E., Giorgioni, M., & Agosta, F. (2019). Fracture simulation parameters of fractured reservoirs: Analogy with outcropping carbonates of the Inner Apulian Platform, southern Italy. *Journal of Structural Geology*, *123*, 18–41. https://doi.org/10.1016/j.jsg.2019.02.007Goldhammer, R., & Harris, M. (1989). *Eustatic controls on the stratigraphy and geometry of the Latemar buildup (Middle Triassic), the Dolomites of northern Italy*. http://archives.datapages.com/data/sepm_sp/SP44/Eustatic_Controls_on_the_Stratigraphy_.pdfGoldham
R. K., Dunn, P. A., & Hardie, L. A. (1990). Depositional cycles, composite sea-level changes, cycle stacking patterns, and the hierarchy of stratigraphic

forcing: Examples from Alpine Triassic platform carbonates. *Bulletin of the Geological Society of America*, *102*(5), 535–562. https://doi.org/10.1130/0016-7606(1990)102<0535:DCCSLC>2.3.CO;2Gramigna, P., Franceschi, M., Gattolin, G., Preto, N., Massironi, M., Riva, A., & Viseur, S. (2013). Geological map of the Middle Triassic Latemar platform (Western Dolomites, Northern Italy). *Journal of Maps*, *9*(2), 313–324. https://doi.org/10.1080/17445647.2013.781311Hancock, P. L. (1985). Brittle microtectonics: principles and practice. *Journal of Structural Geology*, *7*(3–4), 437–457. https://doi.org/10.1016/0191-8141(85)90048-3Hardebol, N. J., Maier, C., Nick, H., Geiger, S., Bertotti, G., & Boro, H. (2015). Multiscale fracture network characterization and impact on flow: A case study on the Latemar carbonate platform. *Journal of Geophysical Research: Solid Earth*, *120*(12), 8197–8222. https://doi.org/10.1002/2015JB012608.ReceivedHarris, M. T. (1994). The Foreslope and toe-of-slope facies of the Middle Triassic Latemar Buildup (the Dolomites, northern Italy). *Sedimentary Research*, 132–145.Harris, M. T. (1993). Reef Fabrics, biotic crusts and syndepositional cements of the Latemar reef margin (Middle Triassic), northern Italy. *Sedimentology*, *40*(3), 383–401. https://doi.org/10.1111/j.1365-3091.1993.tb01342.xHooker, J. N., Laubach, S. E., & Marrett, R. (2013). Fracture-aperture sizedfrequency, spatial distribution, and growth processes in strata-bounded and non-strata-bounded fractures, cambrian mesón group, NW argentina. *Journal of Structural Geology*. https://doi.org/10.1016/j.jsg.2013.06.011Igbokwe, O.A., Mueller, M., Abah, O., Bertotti, G., & Immenhauser, A. (2018). Morphological changes of carbonate deformed clasts in a neogene fault zone. *3rd EAGE Workshop on Naturally Fractured Reservoirs*, *2018-Febru*.Igbokwe, Onyedika Anthony, Mueller, M., Bertotti, G., Timothy, J. J., Abah, O., & Immenhauser, A. (2020). Morphology and topology of dolostone lithons in the regional Carboneras Fault Zone, Southern Spain. *Journal of Structural Geology*, *137*. https://doi.org/10.1016/j.jsg.2020.104073Jacquemyn, C., El Desouky, H., Hunt, D., Casini, G., & Swennen, R. (2014). Dolomitization of the Latemar platform: Fluid flow and dolomite evolution. *Marine and Petroleum Geology*, *55*, 43–67. https://doi.org/10.1016/j.marpetgeo.2014.01.017Jacquemyn, C., Huysmans, M., Hunt, D., Casini, G., & Swennen, R. (2015). Multiscale three-dimensional distribution of fracture-and igneous intrusion-controlled hydrothermal dolomite from digital outcrop model, Latemar platform, Dolomites, northern Italy. *AAPG Bulletin, V*, *99*(5), 957–984. https://doi.org/10.1306/10231414089Korneva, I., Tondi, E., Agosta, F., Rustichelli, A., Spina, V., Bitonte, R., & Di Cuia, R. (2014). Structural properties of fractured and faulted Cretaceous platform carbonates, Murge Plateau (southern Italy). *Marine and Petroleum Geology*. https://doi.org/10.1016/j.marpetgeo.2014.05.004Lamarche, J., Lavenu, A. P. C., Gauthier, B. D. M., Guglielmi, Y., & Jayet, O. (2012). Relationships between fracture patterns, geodynamics and mechanical stratigraphy in Carbonates (South-East Basin, France). *Tectonophysics*, *581*, 231–245. https://doi.org/10.1016/j.tecto.2012.06.042Laubach, S. E., Lamarche, J., Gauthier, B. D. M., Dunne, W. M., & Sanderson, D. J. (2018). Spatial

arrangement of faults and opening-mode fractures. *Journal of Structural Geology*, *108*, 2–15. https://doi.org/10.1016/j.jsg.2017.08.008Laubach, Stephen E. (2003). Practical approaches to identifying sealed and open fractures. *American Association of Petroleum Geologists Bulletin*, *87*(4), 561–579. https://doi.org/10.1306/11060201106Laurenzi, M., & Visona, D. (1996). 40Ar/39Ar Chronology of Predazzo magmatic complex (Southern Alps, Italy). *Proceedings of 78th Riunione Estiva Società Geologica*.Lavenu, A. P. C., Lamarche, J., Salardon, R., Gallois, A., Marié, L., & Gauthier, B. D. M. (2014). Relating background fractures to diagenesis and rock physical properties in a platform-slope transect. Example of the Maiella Mountain (central Italy). *Marine and Petroleum Geology*. https://doi.org/10.1016/j.marpetgeo.2013.11.012Lavenu, A. P. C., Lamarche, J., Texier, L., Marié, L., & Gauthier, B. D. M. (2015). Background fractures in carbonates: Inference on control of sedimentary facies, diagenesis and petrophysics on rock mechanical behavior. Example of the Murge Plateau (southern Italy). *Italian Journal of Geosciences*, *134*(3), 535–555. https://doi.org/10.3301/IJG.2014.58Li, J. Z., Laubach, S. E., Gale, J. F. W., & Marrett, R. A. (2018). Quantifying opening-mode fracture spatial organization in horizontal wellbore image logs, core and outcrop: Application to Upper Cretaceous Frontier Formation tight gas sandstones, USA. *Journal of Structural Geology*, *108*, 137–156. https://doi.org/10.1016/j.jsg.2017.07.005Manzocchi, T. (2002). The connectivity of two-dimensional networks of spatially correlated fractures. *Water Resources Research*. https://doi.org/10.1029/2000wr000180Marangon, A., Gattolin, G., Della Porta, G., & Preto, N. (2011). The Latemar: A flat-topped, steep fronted platform dominated by microbialites and synsedimentary cements. *Sedimentary Geology*, *240*(3–4), 97–114. https://doi.org/10.1016/j.sedgeo.2011.09.001Morley, C. K., & Nixon, C. W. (2016). Topological characteristics of simple and complex normal fault networks. *Journal of Structural Geology*, *84*, 68–84. https://doi.org/10.1016/j.jsg.2016.01.005Mueller, M., Jacquemyn, C., Walter, B. F., Pederson, C. L., Schurr, S. L., Igbokwe, O. A., Jöns, N., Riechelmann, S., Dietzel, M., Strauss, H., & Immenhauser, A. (2021). Constraints on the preservation of proxy data in carbonate archives – lessons from a marine limestone to marble transect, Latemar, Italy. *Sedimentology*. https://doi.org/10.1111/SED.12939Nixon, C W, Sanderson, D. J., Dee, S. L., Bull, J. M., Humphreys, R. J., & Swanson, M. H. (2014). Fault interactions and reactivation within a normal-fault network at Milne Point, Alaska. *AAPG Bulletin*, *98*(10), 2081–2107. https://doi.org/10.1306/04301413177Nixon, Casey W., Nærland, K., Rotevatn, A., Dimmen, V., Sanderson, D. J., & Kristensen, T. B. (2020). Connectivity and network development of carbonate-hosted fault damage zones from western Malta. *Journal of Structural Geology*, *141*, 191–8141. https://doi.org/10.1016/j.jsg.2020.104212Nixon, Casey W., Vaagan, S., Sanderson, D. J., & Gawthorpe, R. L. (2019). Spatial distribution of damage and strain within a normal fault relay at Kilve, U.K. *Journal of Structural Geology*, *118*(March 2018), 194–209. https://doi.org/10.1016/j.jsg.2018.10.016Nyberg, B., Nixon, C. W., & Sanderson, D. J. (2018). NetworkGT: A GIS tool

for geometric and topological analysis of two-dimensional fracture networks. *Geosphere*. https://doi.org/10.1130/GES01595.1Panza, E., Agosta, F., Rustichelli, A., Zambrano, M., Tondi, E., Prosser, G., Giorgioni, M., & Janiseck, J. M. (2016). Fracture stratigraphy and fluid flow properties of shallow-water, tight carbonates: The case study of the Murge Plateau (southern Italy). *Marine and Petroleum Geology*, *73*, 350–370. https://doi.org/10.1016/j.marpetgeo.2016.03.022Pascal, C., & Cloetingh, S. A. P. L. (2009). Gravitational potential stresses and stress field of passive continental margins: Insights from the south-Norway shelf. *Earth and Planetary Science Letters*, *277*(3–4), 464–473. https://doi.org/10.1016/j.epsl.2008.11.014Petrullo, A. V., Agosta, F., Prosser, G., & Rizzo, E. (2017). Cenozoic tectonic evolution of the northern Apulian carbonate platform (southern Italy). *Italian Journal of Geosciences*, *136*(2), 296–311. https://doi.org/10.3301/IJG.2017.08Preto, N., Franceschi, M., Gattolin, G., Massironi, M., Riva, A., Gramigna, P., Bertoldi, L., & Nardon, S. (2011). The Latemar: A Middle Triassic polygonal fault-block platform controlled by synsedimentary tectonics. *Sedimentary Geology*, *234*(1–4), 1–18. https://doi.org/10.1016/j.sedgeo.2010.10.010Putz-Perrier, M. W., & Sanderson, D. J. (2008a). Spatial distribution of brittle strain in layered sequences. *Journal of Structural Geology*, *30*(1), 50–64. https://doi.org/10.1016/j.jsg.2007.10.005Putz-Perrier, M. W., & Sanderson, D. J. (2008b). The distribution of faults and fractures and their importance in accommodating extensional strain at Kimmeridge Bay, Dorset, UK. *Geological Society Special Publication*, *299*, 97–111. https://doi.org/10.1144/SP299.6Roberts, S. J., & Nunn, J. A. (1995). Episodic fluid expulsion from geopressured sediments. *Marine and Petroleum Geology*, *12*(2), 195–204. https://doi.org/10.1016/0264-8172(95)92839-ORuffer, T., & Zuhlke, R. (1995). Sequence stratigraphy and sea-level changes in the early to middle Triassic of the Alps: a global comparison. *Sequence Stratigraphy and Depositional Response to Eustatic, Tectonic and Climatic Forcing (B.U. Haq, Ed)*, 161–207. https://doi.org/10.1007/978-94-015-8583-5_7Sanderson, D J, & Nixon, C. W. (2015). The use of topology in fracture network characterization. *Journal of Structural Geology*, *72*, 55–66. https://doi.org/10.1016/j.jsg.2015.01.005Sanderson, David J., & Nixon, C. W. (2018). Topology, connectivity and percolation in fracture networks. *Journal of Structural Geology*. https://doi.org/10.1016/j.jsg.2018.07.011Sanderson, David J., & Peacock, D. C. P. (2019). Line sampling of fracture swarms and corridors. *Journal of Structural Geology*, *122*, 27–37. https://doi.org/10.1016/j.jsg.2019.02.006Shipton, Z. K., & Cowie, P. A. (2003). A conceptual model for the origin of fault damage zone structures in high-porosity sandstone (vol 25, pg 333, 2003). *Journal of Structural Geology*, *25*(8), 1343–1345. https://doi.org/10.1016/S0191-8141(03)00060-9Sibson, R. H. (2003). Brittle-failure controls on maximum sustainable overpressure in different tectonic regimes. *American Association of Petroleum Geologists Bulletin*, *87*(6), 901–908. https://doi.org/10.1306/01290300181Tondi, E. (2007). Nucleation, development and petrophysical properties of faults in carbonate grainstones: Evidence from the San Vito Lo Capo peninsula (Sicily, Italy). *Journal of Structural Geology*, *29*(4), 614–628.

https://doi.org/10.1016/j.jsg.2006.11.006Turcotte, D., & Schubert, G. (2002). Geodynamics, Second Edition. In *Eos, Transactions American Geophysical Union* (Vol. 84, Issue 18). https://doi.org/10.1029/2003eo180009Visona, D. (1997). The Predazzo multipulse intrusive body (Western Dolomites, Italy). *Field and Mineralogical Studies*, *49*, 117–125.

Figures with captions

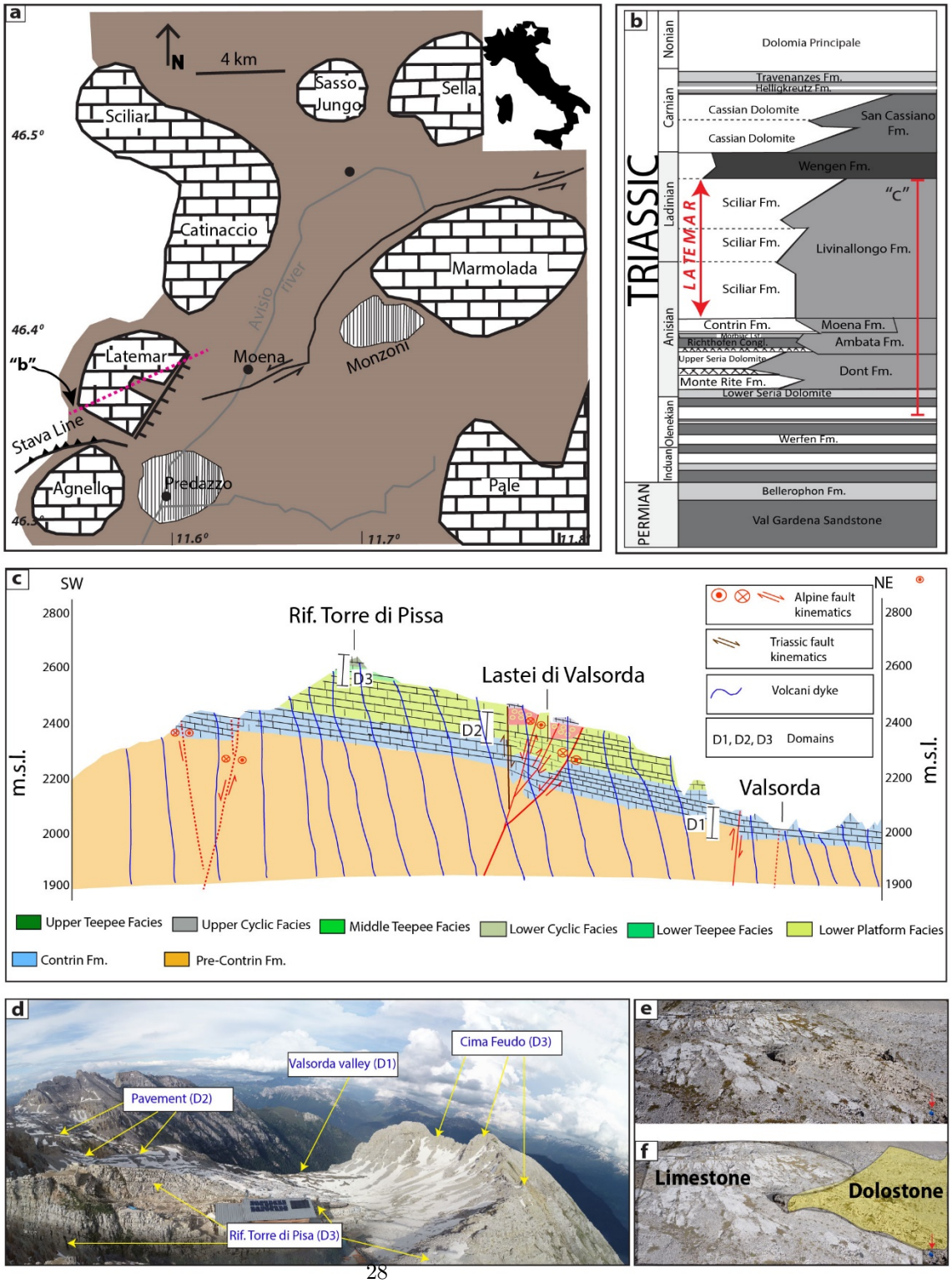
a
N
4 km
Sasso Jungo
Sella
Sciliar
Catinaccio
Marmolada
Avisio river
Latemar
Moena
Monzoni
"b"
Stava Line
Agnello
Predazzo
Pale
46.5°
46.4°
11.6°
11.7°
b
TRIASSIC
PERMIAN
Norian
Carnian
Ladinian
Anisian
Olenekian
Induan
Dolomia Principale
Travenanzes Fm.
Heiligkreutz Fm.
Cassian Dolomite
San Cassiano Fm.
Cassian Dolomite
Wengen Fm.
LATEMAR
Sciliar Fm.
"C"
Sciliar Fm.
Livinallongo Fm.
Sciliar Fm.
Contrin Fm.
Moena Fm.
Ambata Fm.
Richthofen Congl.
Upper Seria Dolomite
Dont Fm.
Monte Rite Fm.
Lower Seria Dolomite
Werfen Fm.
Bellerophon Fm.
Val Gardena Sandstone
c
SW
NE
m.s.l.
2800
2600
2400
2200
2000
1900
Rif. Torre di Pissa
Lastei di Valsorda
Valsorda
D1
D2
D3
Alpine fault kinematics
Triassic fault kinematics
Volcani dyke
D1, D2, D3 Domains
Upper Teepee Facies
Upper Cyclic Facies
Middle Teepee Facies
Lower Cyclic Facies
Lower Teepee Facies
Lower Platform Facies
Contrin Fm.
Pre-Contrin Fm.
d
Cima Feudo (D3)
Valsorda valley (D1)
Pavement (D2)
Rif. Torre di Pisa (D3)
e
f
Limestone
Dolostone

Figure

1. **(A)** Overview of the Latemar and the neighbouring Ladinian carbonate platforms and Upper Ladinian intrusions of the Dolomites (modified after Preto et al., 2011). **(B)** Simplified stratigraphic chart of the Dolomite Mountains, including ranges for cross-section "C." (modified after Jacquemyn et al., 2014) **(C)** Cross-section of Latemar geological map (Fig. 2a) showing the stratigraphic relationship between studied domains (modified after Gramigna et al., 2013). **(D)** Drone image showing the general overview of the studied outcrops (arrows show the outcrops studied). **(E** and **F)** Image acquired from the outcrop pavement at flat-topped Latemar with lime- and dolostone lithologies. Red arrow points to a person with a heigh of 1.73 m

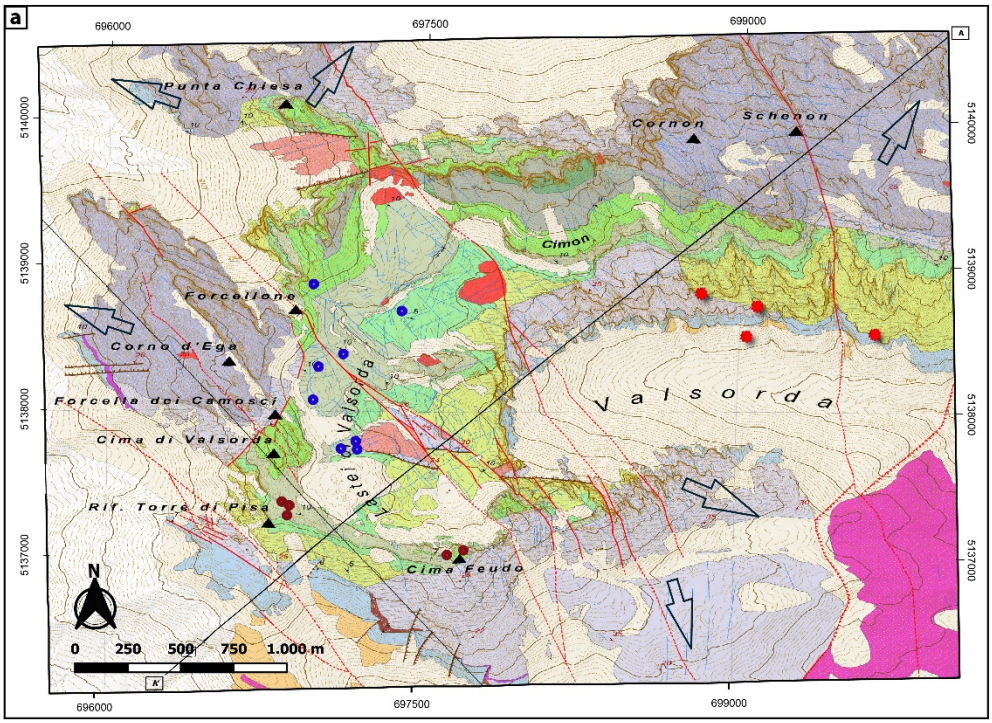
a
696000
697500
699000
5140000
5139000
5138000
5137000
Punta Chiesa
Cornon
Schenon
Cimon
Forcellone
Corno d'Ega
Forcella dei Camosci
Cima di Valsorda
Rif. Torre di Pisa
Cima Feudo
Valsorda
Valsorda
N
0 250 500 750 1.000 m

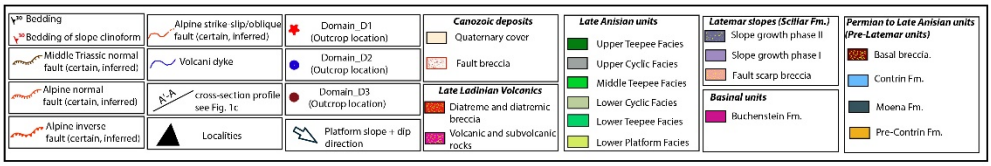
Bedding
Bedding of slope clinoform
Middle Triassic normal fault (certain, inferred)
Alpine normal fault (certain, inferred)
Alpine inverse fault (certain, inferred)
Alpine strike slip/oblique fault (certain, inferred)
Volcani dyke
A-A' cross-section profile see Fig. 1c
Localities
Domain_D1 (Outcrop location)
Domain_D2 (Outcrop location)
Domain_D3 (Outcrop location)
Platform slope + dip direction
Canozoic deposits
Quaternary cover
Fault breccia
Late Ladinian Volcanics
Diatreme and diatremic breccia
Volcanic and subvolcanic rocks
Late Anisian units
Upper Teepee Facies
Upper Cyclic Facies
Middle Teepee Facies
Lower Cyclic Facies
Lower Teepee Facies
Lower Platform Facies
Latemar slopes (Scillar Fm.)
Slope growth phase II
Slope growth phase I
Fault scarp breccia
Basinal units
Buchenstein Fm.
Permian to Late Anisian units (Pre-Latemar units)
Basal breccia.
Contrin Fm.
Moena Fm.
Pre-Contrin Fm.

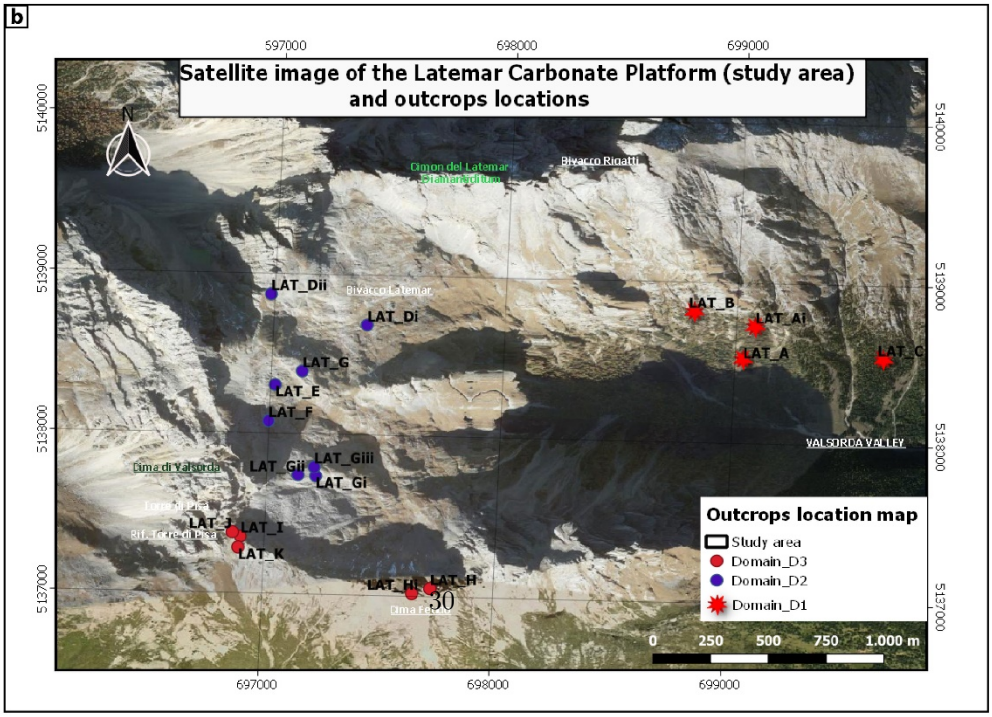
b
597000
698000
699000
5140000
5139000
5138000
5137000
Satellite image of the Latemar Carbonate Platform (study area) and outcrops locations
N
Cimon del Latemar
Bivacco Rinaldi
LAT_Dii
Bivacco Latemar
LAT_Di
LAT_B
LAT_Ai
LAT_A
LAT_C
LAT_G
LAT_E
LAT_F
VALSORDA VALLEY
Cima di Valsorda
LAT_Gii
LAT_Giii
LAT_Gi
Torre di Pisa
LAT_J
LAT_I
Rif. Torre di Pisa
LAT_K
LAT_H
LAT_Hi
Cima Feudo
Outcrops location map
Study area
Domain_D3
Domain_D2
Domain_D1
0 250 500 750 1.000 m
30

Figure 2. **(A)** Geological map of the Middle Triassic Latemar platform, including the study locations (modified after Gramigna et al., 2013). **(B)** The google satellite image of Latemar mountain, including locations of different analyzed outcrops and sampling points.

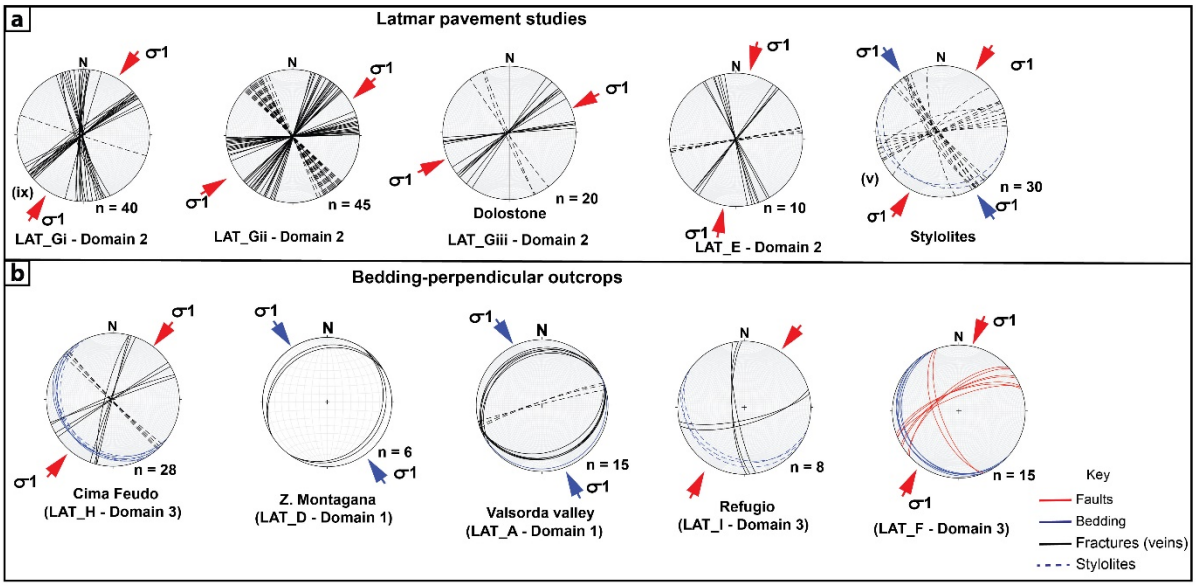

Figure 3. (i through x) Stereoplots show the position of sub-vertical conjugate fractures (veins) and stylolites in 10 representative outcrops (from both bed-parallel and bed-perpendicular) of the study area. Results show two distinct compression phases, namely N-S to NNW-SSE and NE-SW to ENE WSW compressions that characterize the two conjugate systems (CS1 and CS2).

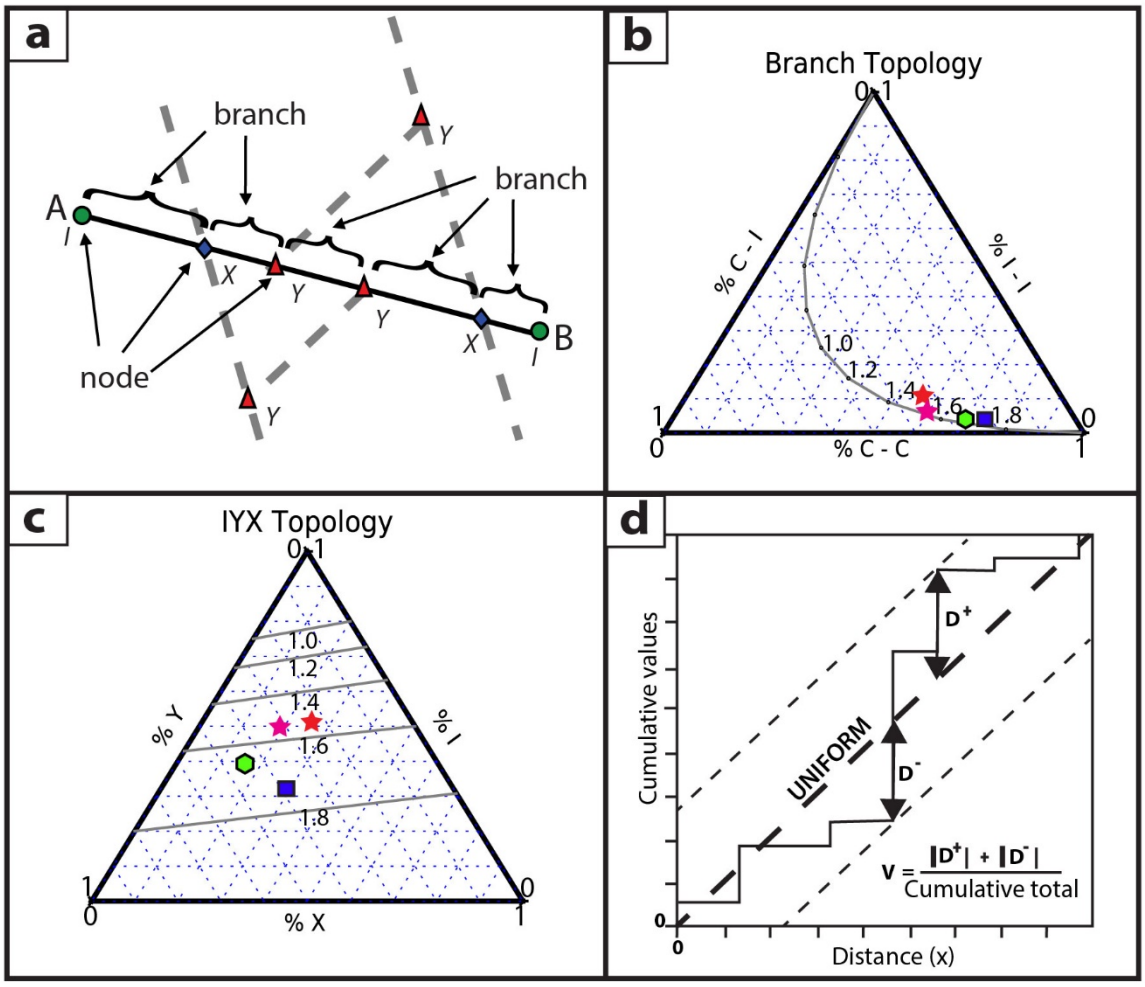

Figure 4. (A) Fracture trace (A-B), with associating intersecting fractures (dashed), showing the arrangement of nodes and branches: I-nodes (green circle); Y-nodes (red triangles); X-nodes (yellow diamonds). (B) Branch classification displaying proportions of different branch types with number 0 – 2 indicating connections per branch (C_B). The curve shows results from the four studied pavements. (C) Values of the number of connections per branch (C_B), indicating the proportion of different nodes, including node proportion of the studied pavements. (D) Schematic example of a cumulative plot along a line transect (solid black line), explaining the maximum deviation above (D^+) and below (D^-) a uniform distribution (thick dashed line) used to calculate the heterogeneity measure (V). Modified after Sanderson and Nixon (2015) and Nixon et al. (2019).

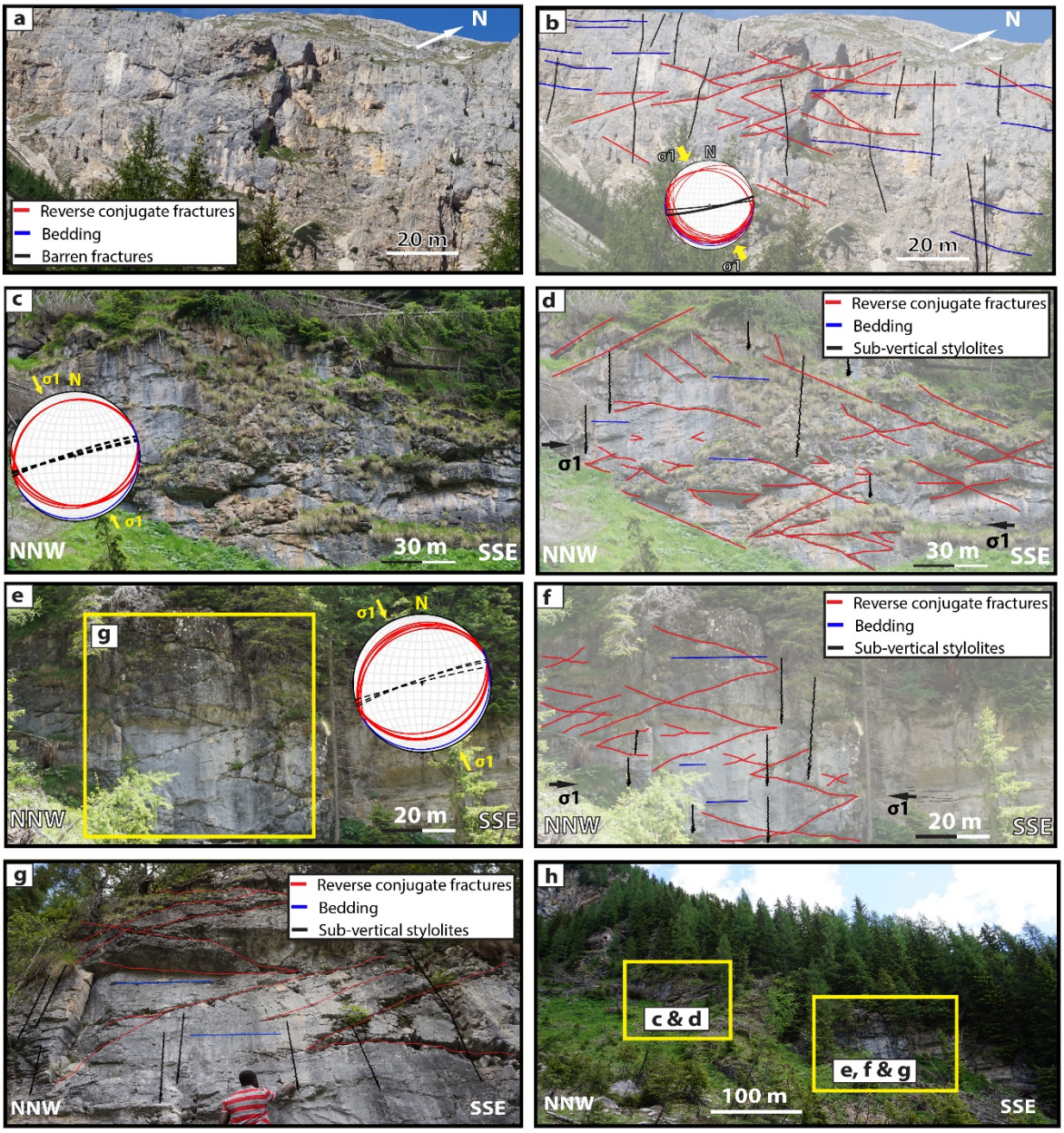

Figure 5. Conjugate fractures, bedding parallel mode I fractures and tectonic stylolites at the base of the Latemar platform (Valsorda area). Each outcrop has stereoplot embedded. (A and B) Panoramic overview of the NNE-SSW flank of the Valsorda valley showing oblique low angle conjugate and sub-vertical

fractures. The conjugate fractures display a NNW-SSE sub-horizontal 1 stress. (C – H) The NNW-SSE flank of the Valsorda valley showing low angle conjugate reverse faults, striking approximately 250-degree ENE-WSW with the horizontal intersection. The principal stress axis determined from the biaxial intersection plane of the conjugate faults lies at NNW-SSE, which belong to conjugate system 1 (CS1).

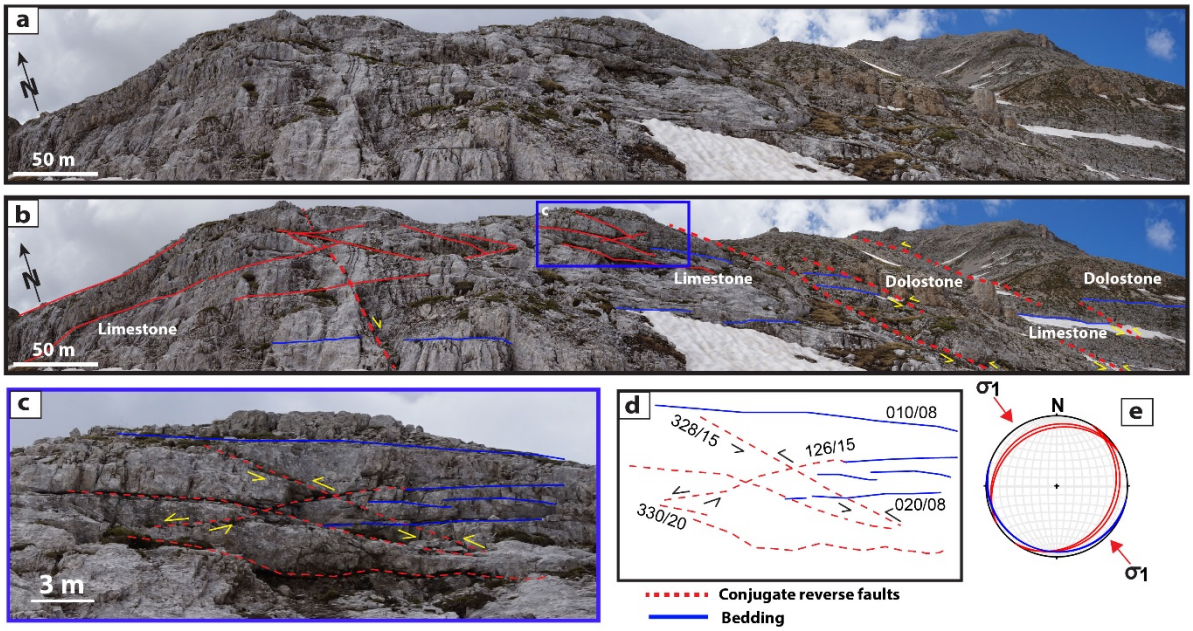

Figure 6. (A and B) Overview of low-angle reverse conjugate fault with fairly developed flat-ramp-flat geometry at San de Montangana in D1 (LAT_D; platform interior). (C and D) Enlargement of B and line diagram of C, respectively, showing the low-angle reverse conjugate faults with sub-horizontal compression direction of ~ NNW-SSE constituting CS1. (E) Stereoplot, showing the position of the conjugate reverse faults and the direction of the sub-horizontal 1 stress.

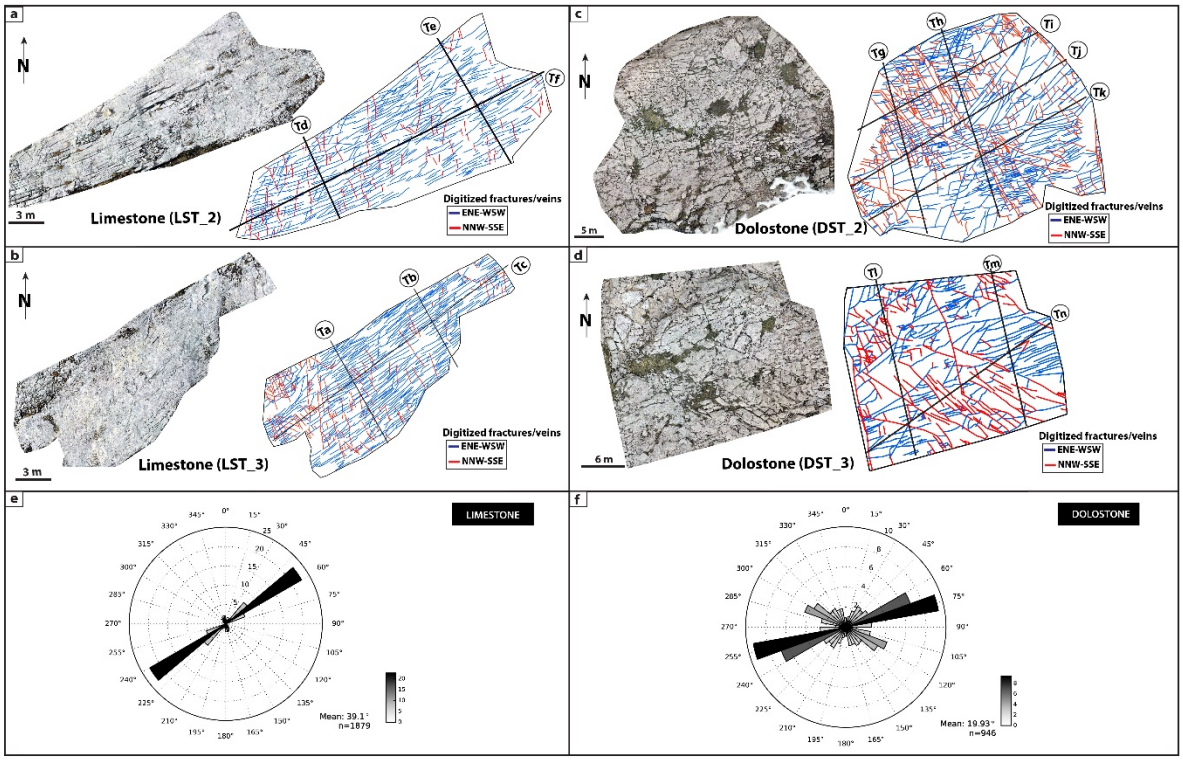

Figure 7. High-resolution 2D drone images coupled with structural interpretation and digitization of the selected limestone and dolostone pavements. The digitized pavements show the position of the NNW-SSE and NE-SW oriented line transects. The directions of fractures are in blue and red, and the fracture frequency measured along each transect illustrate the spatial heterogeneity of the fractures. (A) and (B) show transects (Td – Tf) and (Ta – Tc) that are 10 and 15 m long with a 2 m spacing in limestone pavement, respectively. (C) and (D) shows transects (Tg – Tk) and (Tl – Tn) that are 10 m long with a 2 m spacing in dolostone pavement, respectively. (E) and (F) show rose plots of fractures, indicating significant fractures and/or veins orientations for lime-and dolostone pavements, respectively.

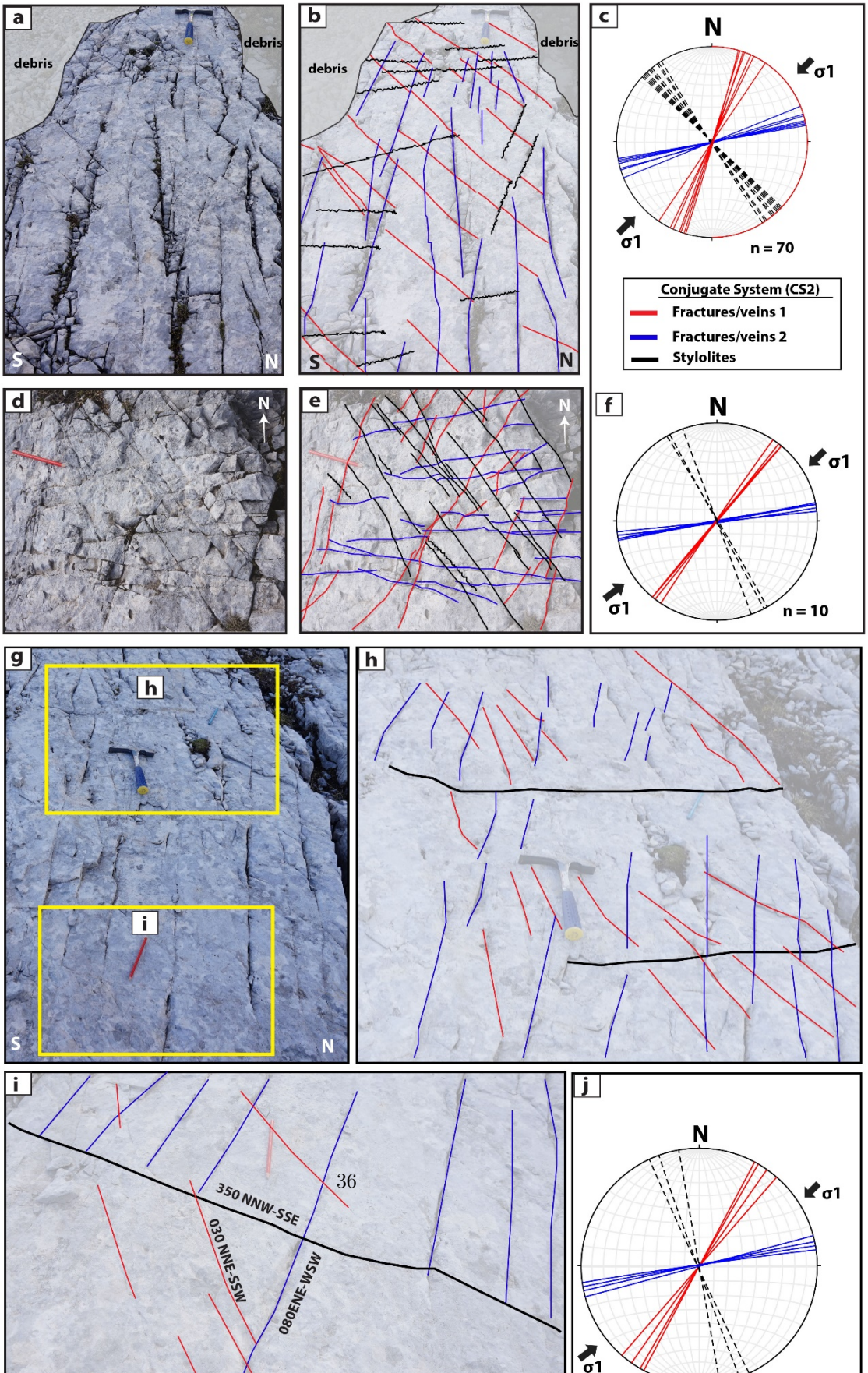
a
debris
debris
S
N
b
debris
debris
S
N
c
N
σ1
σ1
n = 70
Conjugate System (CS2)
Fractures/veins 1
Fractures/veins 2
Stylolites
d
N
e
N
f
N
σ1
σ1
n = 10
g
h
i
S
N
h
i
350 NNW-SSE
030 NNE-SSW
080ENE-WSW
j
N
σ1
σ1

Figure 8. (A-J) Three small-scale limestone pavements in D2 (platform interior; outcrops LAT_Gi and Gii) show conjugate veins with low inter-fault angle associated with approximately NNW-SSE sub-vertical (tectonic) stylolites and an ENE-WSW sub-horizontal 1. The veins and stylolites constitute "conjugate system 2" (CS2; see the description in the text). H and I) Enlargment of G. (C, F, and J) Stereoplots showing the positions of the sub-vertical conjugate veins and tectonic stylolites.

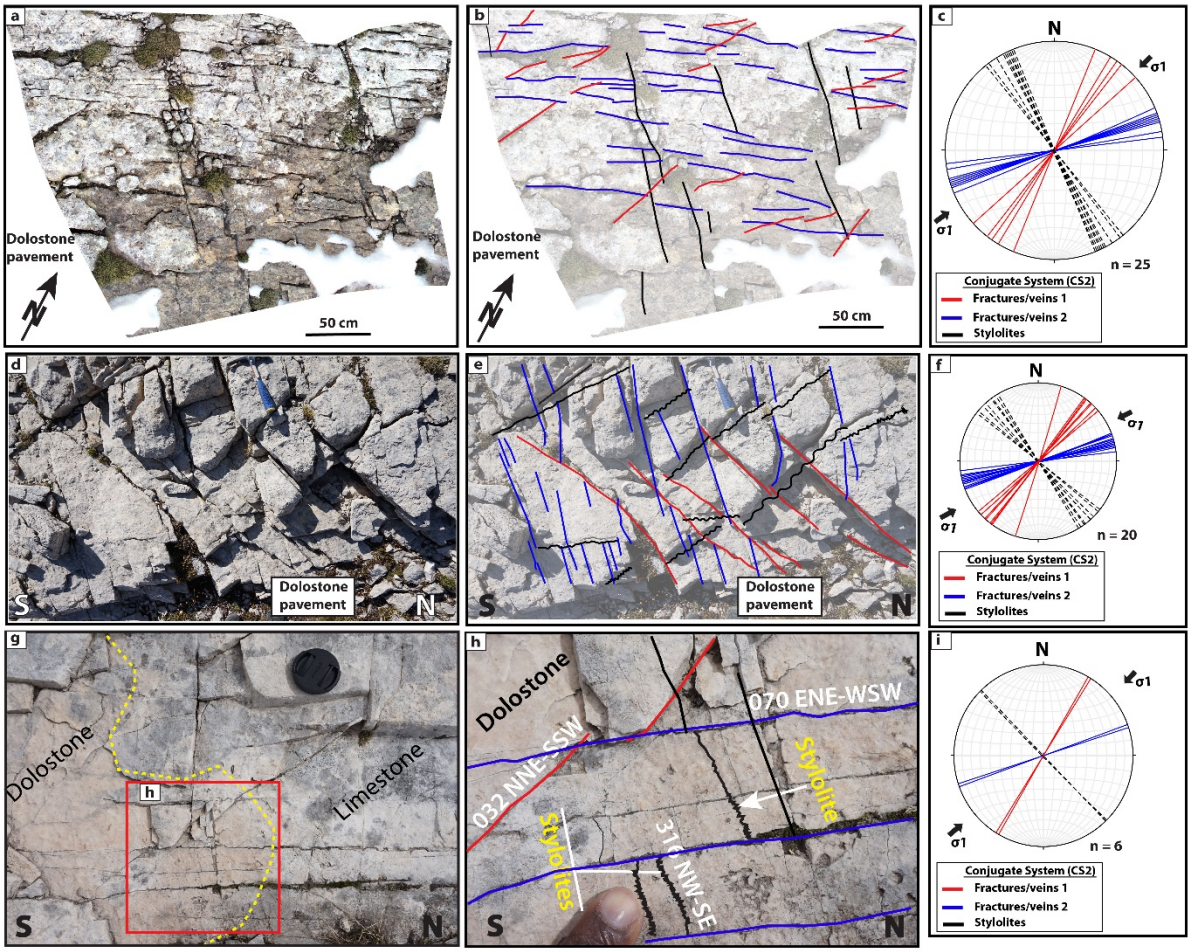

Figure 9. Three small-scale dolostone pavements in D2 (platform interior; LAT_Giii). A,B and D,E) Conjugate fractures/veins with low inter-fault angle associated with approximately NNW-SSE sub-vertical (tectonic) stylolites, and NE-SW to ENE-WSW sub-horizontal 1. The veins and stylolites constitute "conjugate system 2" (CS2; see the description in the text). G,H) Overprinting relations between the conjugate fractures and sub-vertical stylolites. C,F and I) Stereoplots showing the positions of the conjugate fractures/veins and tectonic

stylolites.

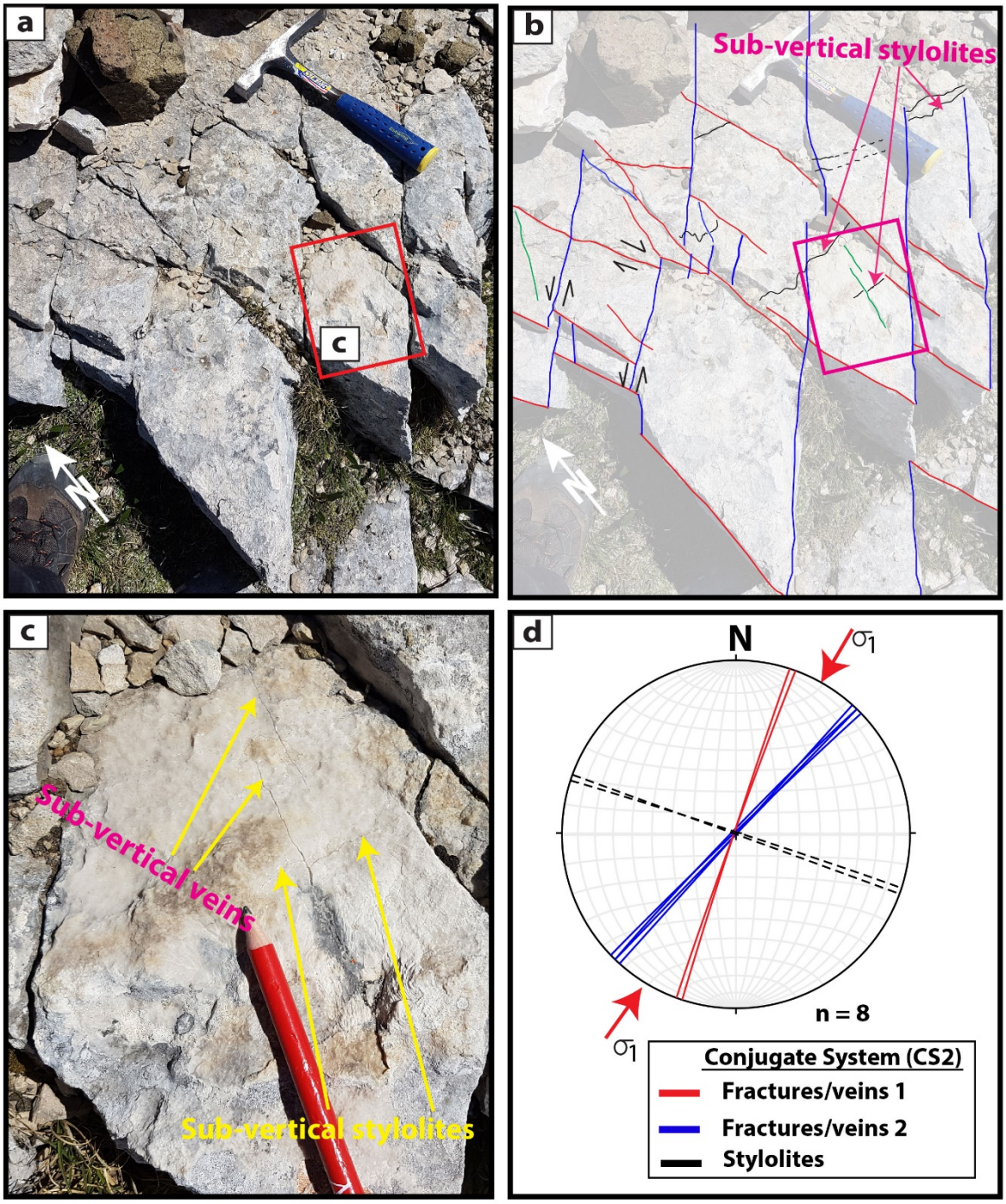
a
c
N
b
Sub-vertical stylolites
N
c
Sub-vertical veins
Sub-vertical stylolites
d
N
σ1
σ1
n = 8
Conjugate System (CS2)
Fractures/veins 1
Fractures/veins 2
Stylolites

Figure 10. A and B) Bedding parallel outcrop in D3 showing conjugate fractures/veins and subvertical stylolites, which belong to the conjugate system 2. The conjugate fractures/veins display a dextral and sinistral sense of movement. C) Enlargement of A, showing the overprinting relationship between the NW-SE sub-vertical stylolite and a later sub-vertical vein.

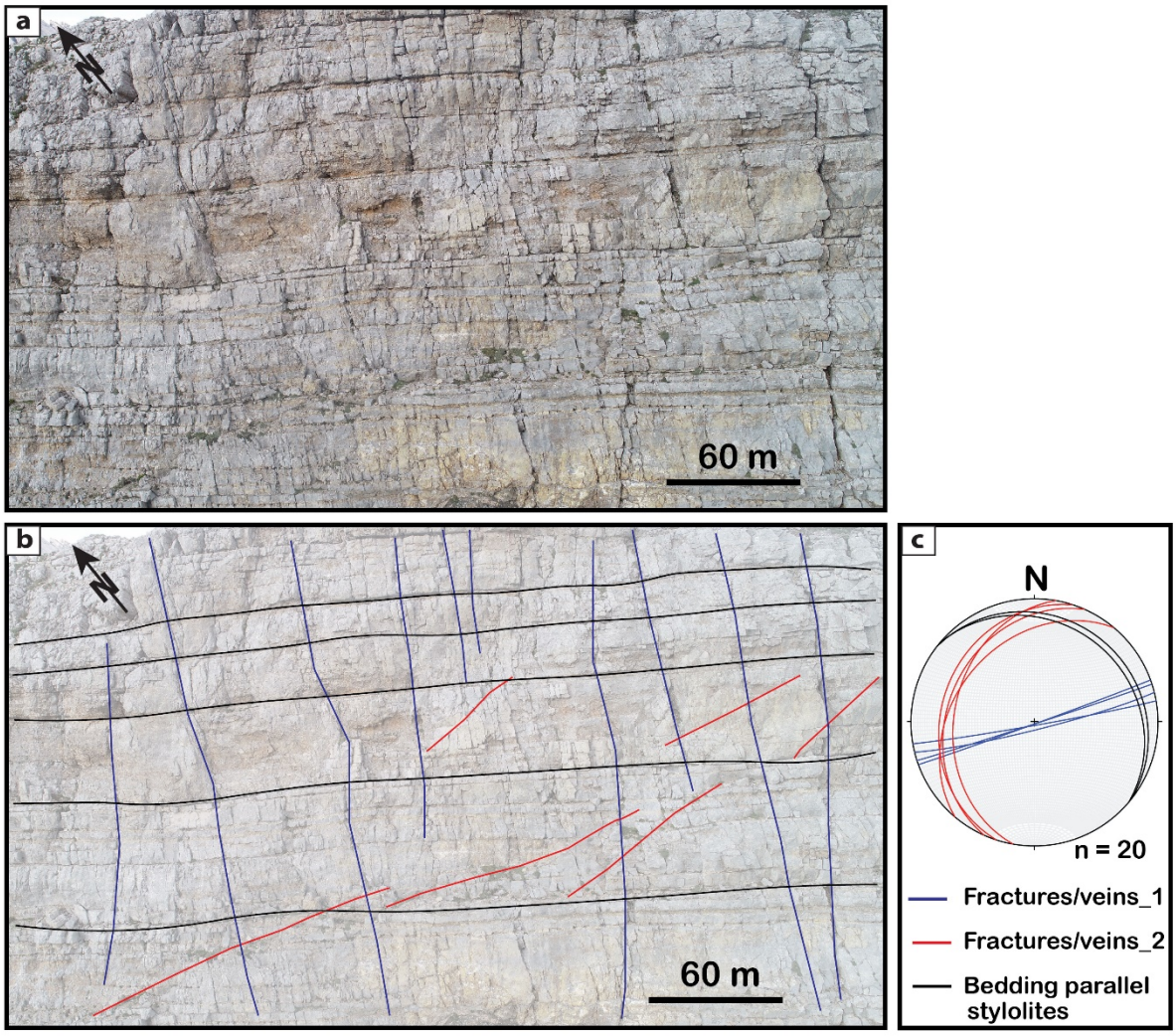

Figure 11. (A) Photograph of one of the studied outcrop in D3 showing ~ 150 x 15 m-long and high vertical wall (LAT_J; at the Rif. Torre di Pisa). B) Structural interpretation of the photograph and the stereoplot presents the fractures and bedding measurements.

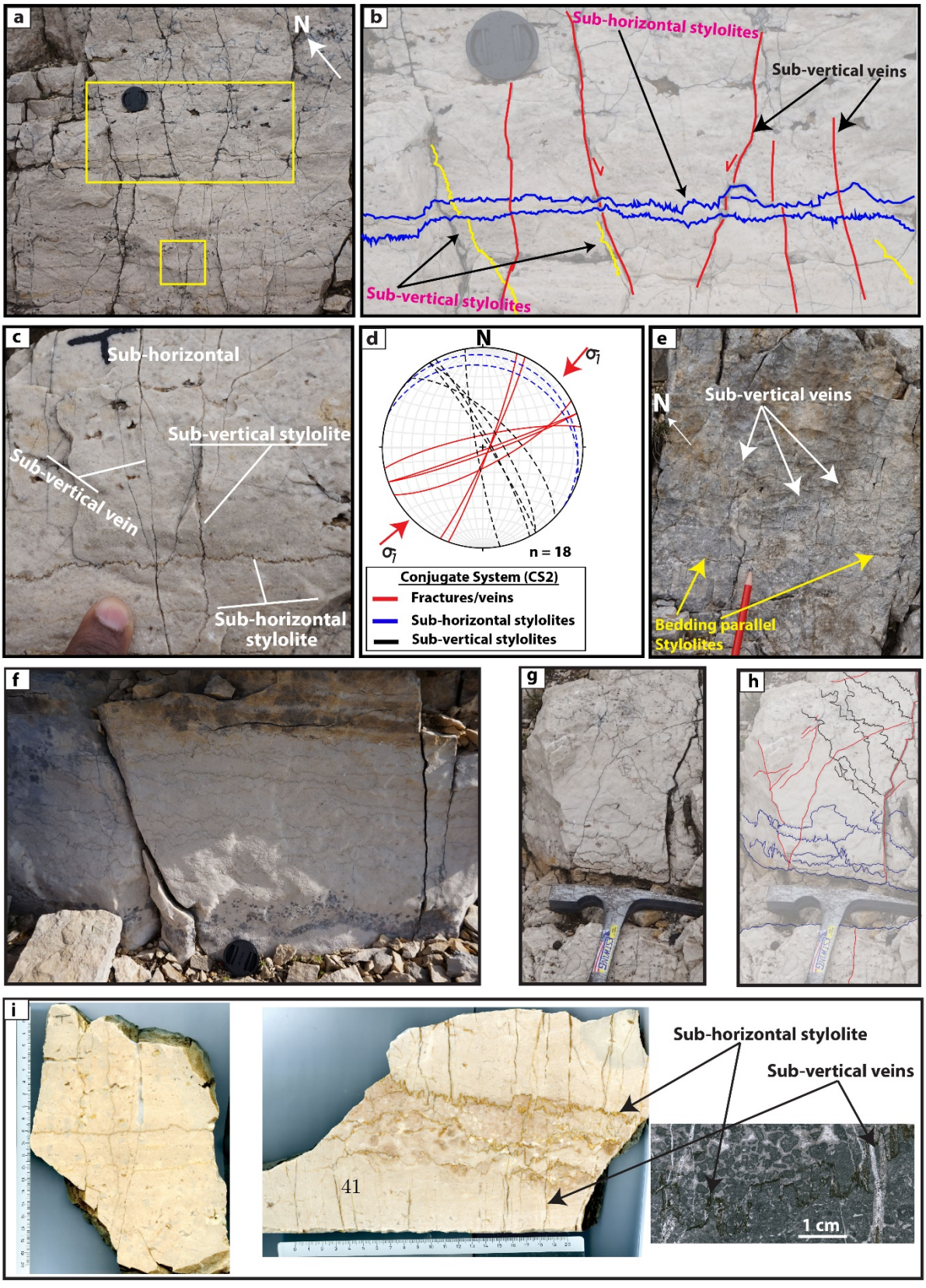
a
N
b
Sub-horizontal stylolites
Sub-vertical veins
Sub-vertical stylolites
c
Sub-horizontal
Sub-vertical stylolite
Sub-vertical vein
Sub-horizontal stylolite
d
N
σ1
σ1
n = 18
Conjugate System (CS2)
Fractures/veins
Sub-horizontal stylolites
Sub-vertical stylolites
e
N
Sub-vertical veins
Bedding parallel Stylolites
f
g
h
i
Sub-horizontal stylolite
Sub-vertical veins
1 cm

Figure 12. Structures observed in the bedding-perpendicular outcrop at the Rifugio station (D3). (A, B and E) Bedding-parallel stylolites are overprinting bedding-perpendicular veins, belonging to the CS2. (B) Enlargement of A, showing that the sub-vertical NNW-SSE stylolites and the conjugate veins, belonging to CS2, are overprinted by the bedding-parallel stylolites. (C) Close-up of A, displays bedding parallel stylolites overprinting the sub-vertical stylolites. The sub-vertical veins and the bedding parallel stylolites appear to mutually crosscut each other. (D) Stereo plot showing the positions of the conjugate veins, sub-vertical and bedding parallel stylolites. (E) Sub-vertical veins overprinted by bedding parallel stylolites. (F) Hand-specimen and plane polarized light image showing cross-cutting relation between the sub-vertical veins and bedding parallel, indicating that fracturing and vein infill predated burial stylolite formation.

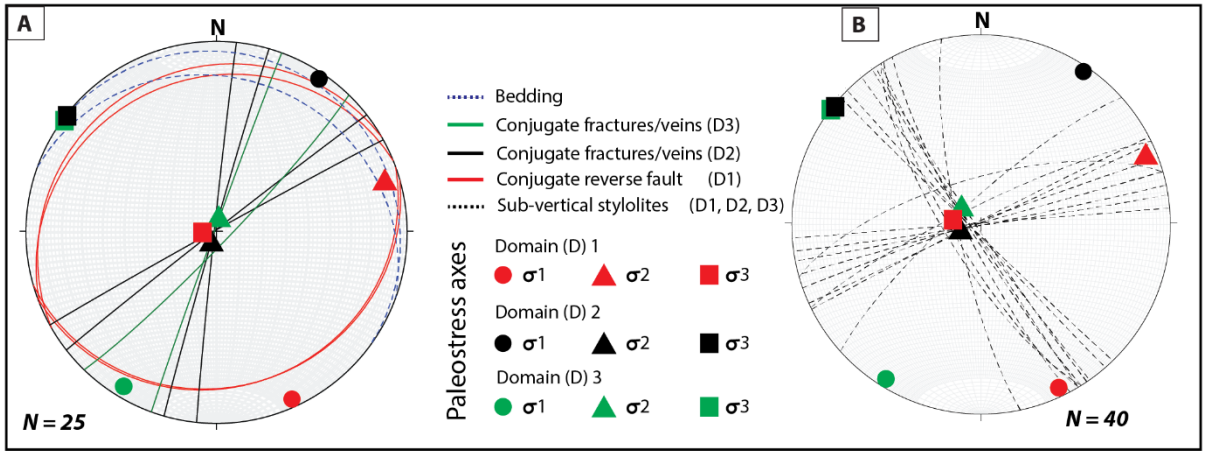

Figure 13. A and B. Summary showing the cumulative result of the representative relevant structural elements observed in each domain of the Latemar platform. 1 = maximum principal stress; 2 = intermediate principal stress; 3 = minimum principal stress.

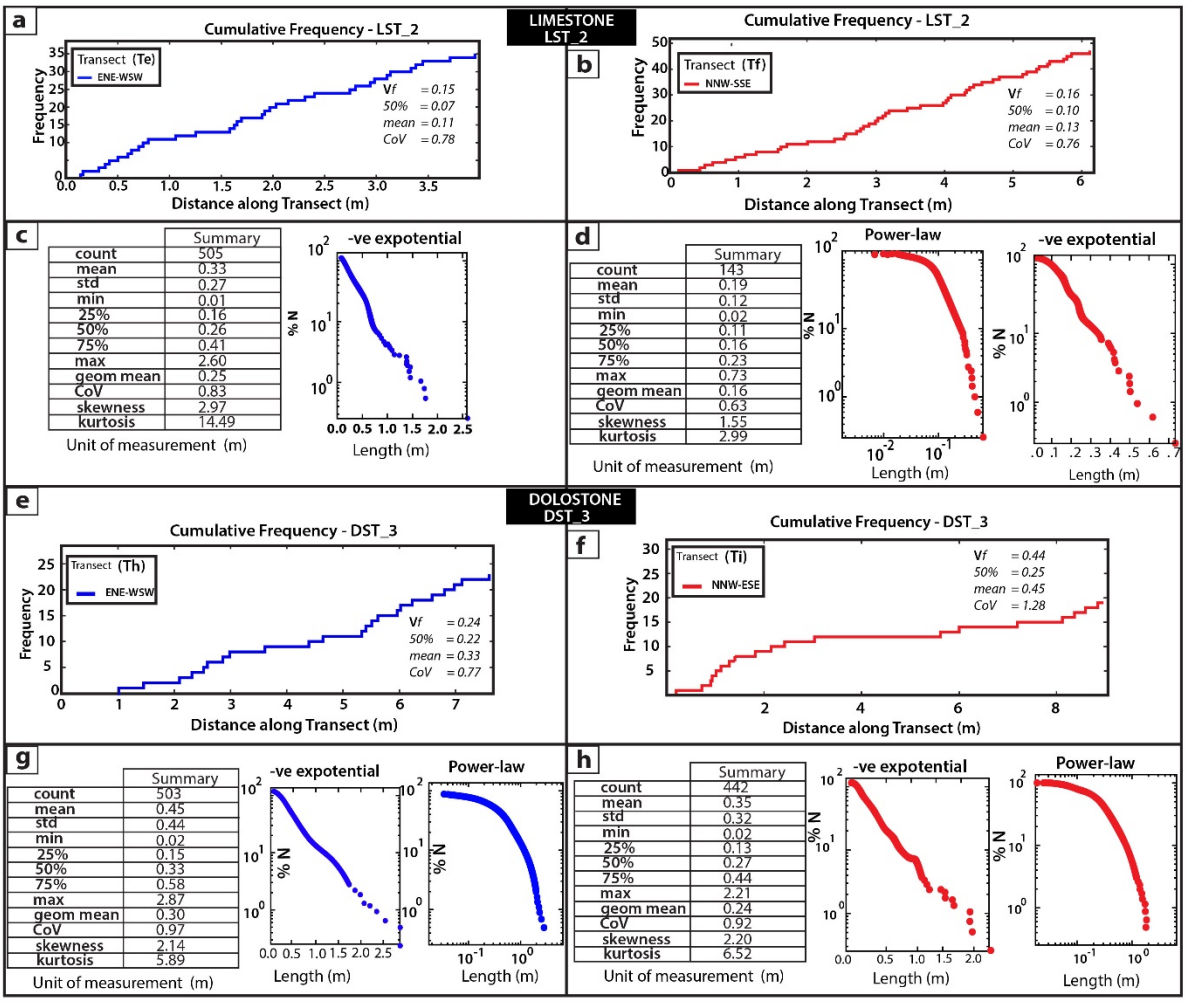

Figure 14. The line transects of cumulative frequency show the distribution in space and deformation of the two distinct fracture clusters in lime- and dolostone pavements and distribution analysis of fracture lengths using a series of cumulative frequency plots and a table of statistics for the fracture/vein network. Examples of non-normalized cumulative plots of fracture/vein frequency; (A) and (B) for transects (Te) and (Tf) of the limestone pavement (see Fig. 7a for the transect). (E) and (F) for transects (Tm) and (Tn) of the dolostone pavement (see Fig. 7d for the transect). Plots in (C and D, and G and H) show the normalized cumulative number of fractures and the range of fracture lengths measured in lime- and dolostone pavements for the ENE-WSW and the NNW-SSE clusters, respectively. Note the negative exponential and power-law fits for both fracture clusters in the lime- and dolostone pavements.

Uniform distribution for fracture frequency is shown for the ENE-WSW (solid

blue line) and NNW-SSE (solid red line) fractures within the distance along the transect. Calculated values for heterogeneity measures V_f for all the fractures and/or veins are listed for each plot.

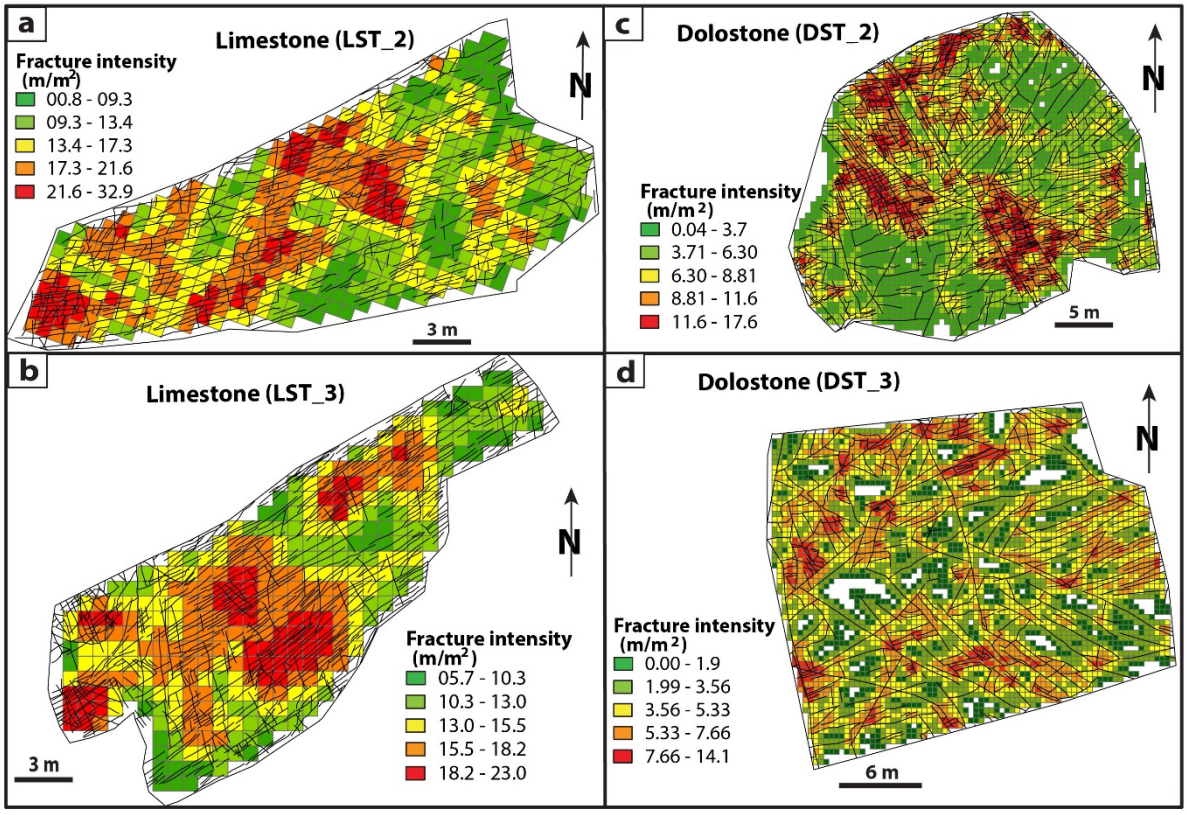

Figure 15 Fracture trace and intensity maps of the representative lime- and dolostone pavements exposed at the flat-topped Latemar. (A and B) show limestone local fracture intensity, ranging from 09.3 to 32.9 m/m^2 (LST_2) and 10.3 to 23.0 m/m^2 (LST_3). (C and D) show dolostone local fracture intensity, ranging from 3.7 to 17.6 m/m^2 (DST_2) and 1.9 to 14.1 m/m^2 (DST_3).

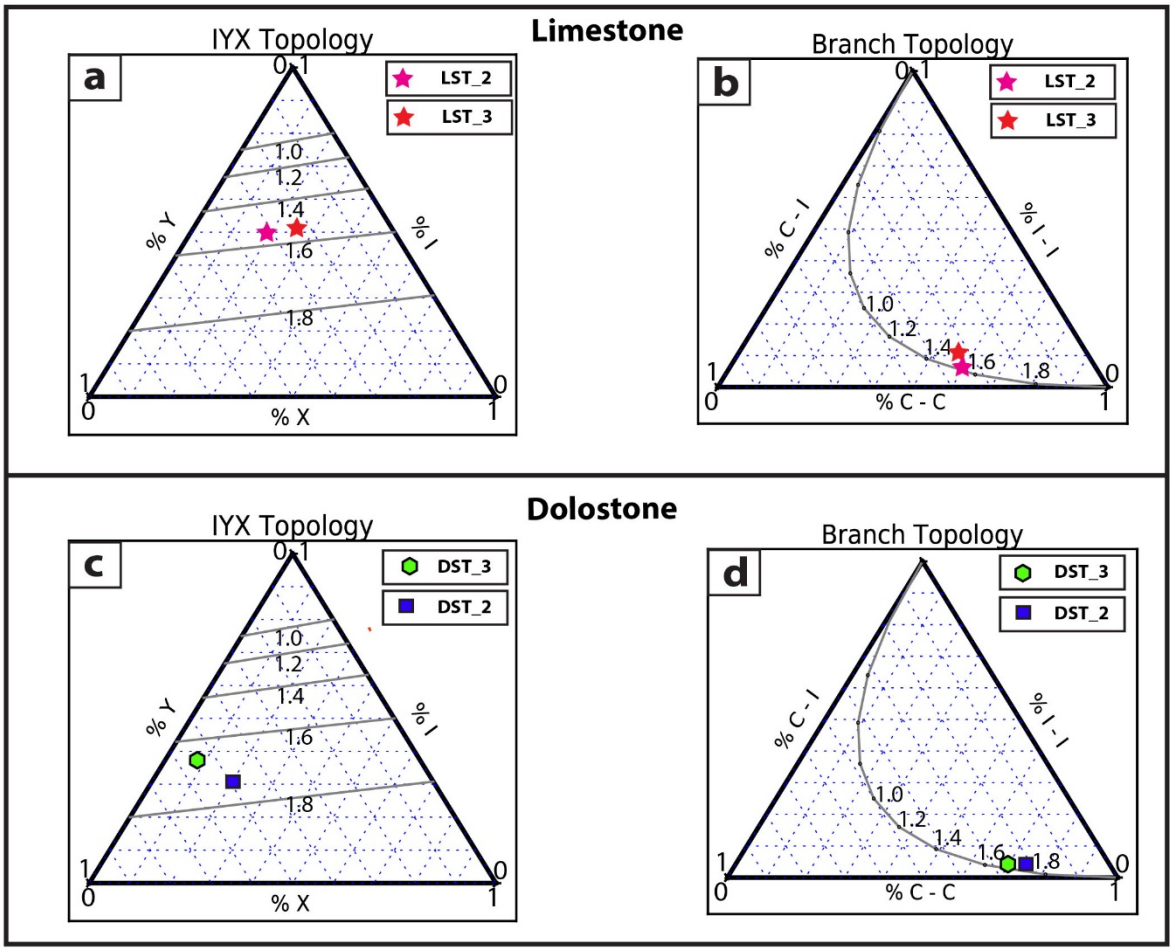

Figure 16. Node and branch triangular plots of the representative lime- and dolostone pavements. Limestone pavements are presented in A) and B), whereas dolostone pavements are shown in C) and D). The node triangles (left) explain the proportions of I-, Y- and X-nodes mapped for each pavement. The branch triangles (right) illustrate the proportion of II-, IC-, and CC-branches mapped for each pavement.

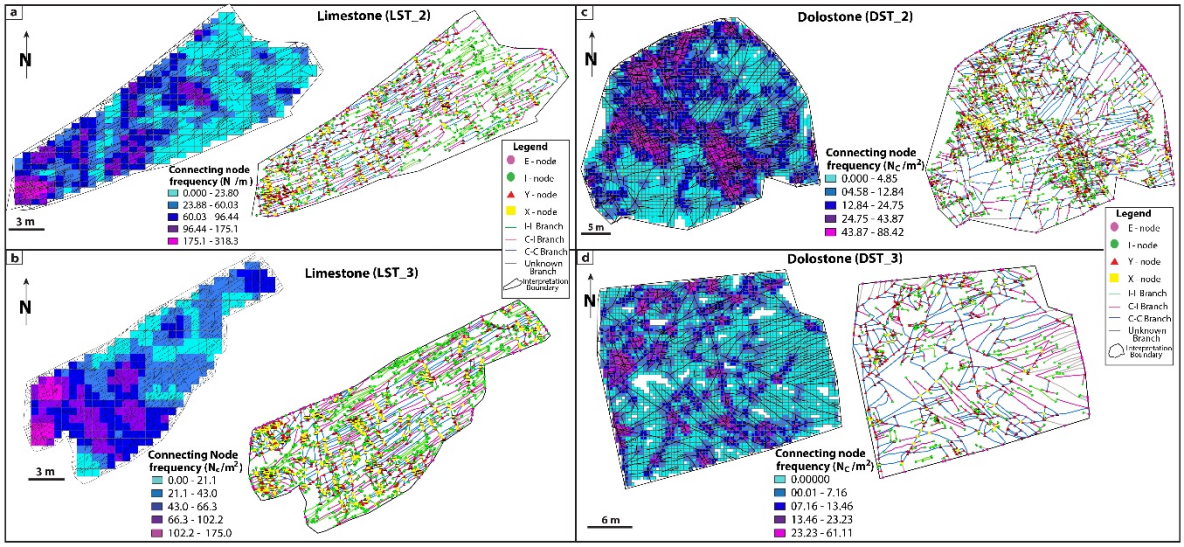

Figure 17. (A) through (D) Map showing topological parameter "connecting node frequency" and their relations within the lime- and dolostone pavements.

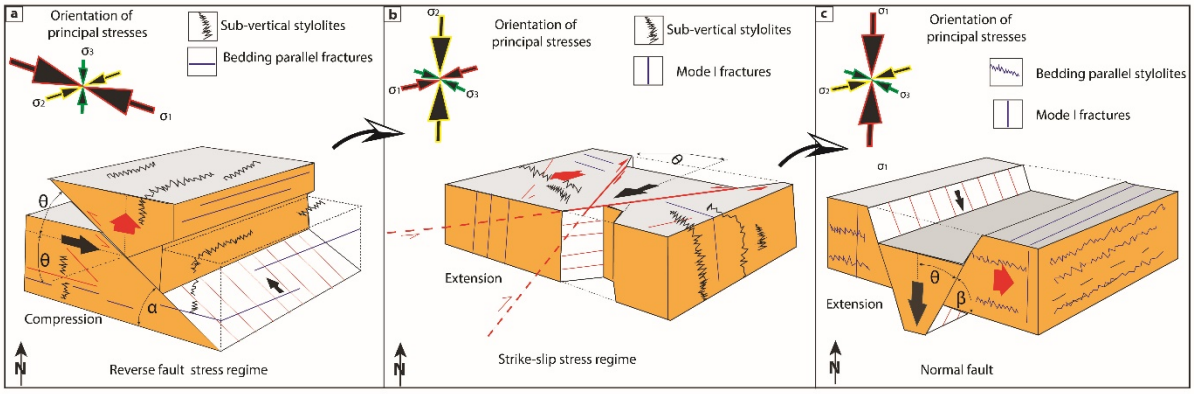

Figure 18. Interpretative sketch reporting the development of the structural elements and stress history in the Latemar platform inferred from the field-based datasets. The stress history is explained following the Andersonian stress regimes (A through C), showing ideal fault regimes and the orientation of their different principal stresses. Modified from (Anderson, 1905)

Tables

Table 1. List of some of the main outcrops and structural stations in the Latemar platform used for this study. Main outcrop information from left to right column: Outcrop/station name, GPS location, and Domains (D1, D2, and D3 represent the first, second and third domains, respectively). See Figs. 2 and

3 for the information on the number of data (outcrops), conjugate systems and bedding orientation, respectively.

S/N	Outcrop stations	GPS locations	Domains
1	LAT_A	N46° 22' 14'' E11° 35' 15''	D1
2	LAT_B	N46° 22' 26'' E11° 35' 03''	D1
3	LAT_C	N46° 22' 35'' E11° 35' 54''	D1
4	LAT_D	N46° 22' 28'' E11° 33' 89''	D1/D2
5	LAT_E	N46° 22' 09'' E11° 33' 46''	D2
6	LAT_F	N46° 22' 13'' E11° 32' 69''	D2
7	LAT_G	N46° 21' 87'' E11° 33' 46''	D2
8	LAT_H	N46° 21' 24'' E11° 34' 14''	D3
9	LAT_I	N46° 21' 66'' E11° 33' 57''	D3
10	LAT_J	N46° 21' 47'' E11° 33' 56''	D3

Table 2. Node and branch data derived from the lime- and dolostone fractured networks shown in Figs. 16 and 17 outcrops (pavements).

Outcrops	**I**	**Y**	**X**	**No. of nodes**	**No. of branches**	**Connections per branch**	II	IC
DST_2	855	1350	447	2652	3346.5	1.7	58	734
DST_3	324	410	69	803	915	1.6	40	224
LST_2	646	385	228	1259	1356.5	1.5	109	417
LST_3	825	382	427	1634	1839.5	1.6	119	572